
Unterschrift BetreuerIn



TECHNISCHE
UNIVERSITÄT
WIEN
Vienna University of Technology

DIPLOMARBEIT

The Development and Implementation of a Fibre Detector and Advanced Data Acquisition for the ASACUSA Antihydrogen Detector

Ausgeführt am Stefan-Meyer-Institut für subatomare Physik
der Österreichischen Akademie der Wissenschaften

unter der Anleitung von
Hon.-Prof. Dipl.-Phys. Dr. Eberhard Widmann

Eingereicht an der Technischen Universität Wien,
Fakultät für Physik,

von

Markus Fleck, BSc.

Leegasse 10/6, 1140 Wien

Wien, am 18. Jänner
2018

Unterschrift StudentIn

Kurzfassung

Die moderne theoretische Teilchenphysik arbeitet vor allem im sogenannten Standardmodell der Teilchenphysik. Dieses theoretische Rahmenwerk ist schon in einer Vielzahl von Experimenten bestätigt worden, wie zum Beispiel mit der Entdeckung des Higgsteilchens im Jahr 2013. Ein zentraler Punkt im Standardmodell ist, dass es sich stark auf Symmetrien stützt. Speziell die CPT -Symmetrie (gleichzeitige Ladungsumkehr, Paritätstransformation und Zeitumkehr) darf in diesem Modell nicht gebrochen sein. Die Untersuchung dieser Symmetrie bietet einen Zugang zu entweder weiterer Verifikation des Standardmodells, oder zu Physik abseits des Standardmodells. Am Antiproton Decelerator (**AD**) der Europäischen Organisation für Kernforschung (**CERN**) versucht die ASACUSA Kollaboration die Differenz zwischen der Hyperfeinstrukturaufspaltung des herkömmlichen Wasserstoffs und seines Antimateriegegenstücks, des Antiwasserstoffs, zu messen. Eine solche Messung bietet einen direkten Test der CPT -Symmetrie.

Dafür nutzt ASACUSA ein Spektroskopiesystem nach der Rabi-Methode, das aus einer polarisierten Antiwasserstoffquelle, einer Mikrowellenkavität, einem analysierenden Sextupolmagneten sowie einem Detektor besteht. Dieser Detektor ist der Hauptfokus dieser Arbeit. Bisher war der Detektor dazu im Stande, den Ort der Annihilation auf dem zentralen Target, die Energiedeposition, sowie die Winkel der bei der Annihilation entstehenden Pionen, bzw. deren Spuren in einer Ebene normal zur Strahlrichtung aufzunehmen. Das Hauptproblem der Analyse der Daten ist die Unterscheidung von tatsächlichen Antiwasserstoffereignissen, kosmischen Strahlen und Signalen von Annihilationen abseits des Targets, die von über- und unterfokussierten Antiwasserstoff und Antiprotonen stammen. Durch die hohe Anzahl von Hintergrundereignissen und der unzureichenden Positionsauflösung sind die vorhandenen Informationen oft nicht ausreichend um eine klare Trennung festzulegen.

In der vorliegenden Arbeit wurde eine zusätzliche Komponente für das Detektorsystem entwickelt und implementiert, die es ermöglicht, genaue Positionsinformationen in der Strahlrichtung zu erhalten, um uneigentliche Ereignisse zuverlässiger auszuschließen. Ein Schwerpunkt sind die konstruktiven Details des neuen Detektors, ein weiterer sind die Systeme zur Datenaufnahme und Detektorkontrolle, die beide modifiziert und teilweise neu geschrieben wurden. Weiters werden der Designprozess und Testdaten präsentiert.

Abstract

Modern theoretical particle physics mostly operates within the so called standard model of particle physics. This framework has been verified by a number of experiments, for instance the discovery of the Higgs boson in 2013. A central point of the standard model is its reliance on symmetries. Especially the CPT symmetry (simultaneous charge conjugation, parity transformation and time reversal) has to be unbroken within this model. The investigation of this symmetry provides an approach to either further verification of the the standard model, or shines a light on physics beyond the standard model. At the Antiproton Decelerator (**AD**) of the European Organisation for Nuclear Research (**CERN**) the ASACUSA collaboration intends to measure the difference between the hyperfine splitting of hydrogen and that of its antimatter counterpart, antihydrogen. Such a measurement provides a direct test of the CPT symmetry.

To accomplish this, ASACUSA uses a Rabi-type spectroscopy setup, consisting of a polarised antihydrogen source, a microwave cavity, an analysing sextupole magnet, as well as a detector. This detector is the main focus of this thesis. So far the detector was able to record the position of the annihilation on the central target, the energy deposition and the angles of the pions produced in the annihilation, or rather their tracks in a plane perpendicular to the beam direction. The main problem in the data analysis is the differentiation of actual antihydrogen events, cosmic rays, and signals of annihilations besides the target, caused by over- or underfocused antihydrogen and antiprotons. Due to the high amount of background events and the inadequate position distribution, especially in beam direction, a clear distinction is often not possible.

In this thesis, an additional component for the detector system that enables precise spatial resolution in the beam direction was developed and implemented, so that false events can definitely be discriminated. One focus of this work will be the constructional details of the new detector, another one the data acquisition and slow control systems, which have been modified and partially rewritten. Also presented are the design process as well as some test data.

Contents

1. Introduction	3
1.1. Motivation	4
2. Physics Fundamentals	6
2.1. The Hyperfine Structure of (Anti-)Hydrogen	6
2.2. Minimal Standard Model Extension	7
2.3. Antihydrogen Annihilation	9
2.4. Plastic scintillators	9
3. Experimental Setup	12
3.1. Rabi Method	12
3.2. Beam line	13
3.2.1. Accelerator complex	13
3.2.2. Antihydrogen Source	13
3.2.3. Spectroscopy apparatus	18
3.3. Detector	18
3.4. Detection of Antihydrogen Annihilation Events	20
3.4.1. Experimental Background	22
3.4.2. Cosmic Background	22
4. The Hodoscope Fibre Detector	25
4.1. Concept and Design	25
4.2. Prototype Measurements	28
4.3. Assembly	32
5. Data Acquisition	40
5.1. Basic DAQ System	40
5.1.1. MIDAS	41
5.1.2. Analyser	44
5.1.3. SiPM Amplification and Slow Control	45
5.2. Advancements in the DAQ System	46
5.2.1. Accessing the V1190 TDC Module	46
5.2.2. Pre-analysing the Fibre Data	53
5.2.3. Nanosecond Time Stamps	56
5.2.4. New Amplifiers and Slow Control	57

Contents

6. Summary and Outlook	63
6.1. Summary	63
6.2. Outlook	65
Appendix	67
A. Used Acronyms	68
B. Materials and Devices	70
C. Additional Tables, Listings and Figures	71
C.1. Specifications of used Fibres and SiPM	71
C.2. Measurements during Design and Assembly	72
C.3. MIDAS Data banks	76
C.4. Structure of the ROOT Trees	77
C.5. Trigger flow diagrams	80
C.6. Fibre Detector Channel Mapping	82
C.7. Microcontroller commands in <i>v1190.c</i>	83
D. Listings	84
E. List of Figures	85
F. List of Tables	88
G. Bibliography	90

1. Introduction

Modern particle physics mainly operates within the framework of the so called standard model of particle physics. The standard model predicted correctly heavier quarks and the Higgs boson, as well as many more particles, making it one of the most successful models in physics to date [1]. Within the standard model, symmetries are very prevalent, thus they are an actively investigated topic both in theoretical and experimental physics. So far, both the symmetry under parity transformation \mathcal{P} and under a combination of charge conjugation and parity transformation \mathcal{CP} were shown to be broken for certain processes in high precision experiments by Wu [2], and Cronin and Fitch [3] respectively.

One of the most fundamental symmetries, the symmetry under a combination of charge conjugation, parity transformation and time reversal, \mathcal{CPT} , however, was never found to be broken so far. If all three transformations are applied, so if all involved charges are reversed, the momenta are reversed (a consequence of the time reversal) and the process is inverted through a point (parity transformation), the process follows the same physical laws as a non-transformed process. The particles involved in such "mirrored" processes are called antiparticles, or, more general, antimatter.

Antimatter was first discovered in the shape of the positron, the electron with an opposite charge, in 1932 by Anderson [4], after being proposed by Dirac in 1928 [5]. A few years later, the anti-partners of the nucleons, the antiproton and the antineutron, were discovered in 1955 by Chamberlain [6] and 1956 by Cork [7] respectively. Since then, anti-nuclei have also been observed [8–10].

The relationship between particles and antiparticles makes antimatter a well suited tool for the investigation of the \mathcal{CPT} -symmetry, since differences between them would be strong hints for a violation of the \mathcal{CPT} -invariance. An experiment comparing the properties of hydrogen with those of antihydrogen seems especially promising, as hydrogen is one of the best known elements and antihydrogen is, comparatively speaking, an easy to produce anti-element.

Although the production of antiparticles and antiatoms is possible in high-energy regimes, antihydrogen produced in such a manner is in a highly excited state and very hot, therefore unsuitable for precision experiments. To provide a source of cold antimatter, the European Organisation for Nuclear Research (Conseil Européene pour la Recherche Nucléaire, CERN) commissioned the Antiproton Decelerator (AD) as part of its accelerator complex in 2000. Using the AD beam of antiprotons and an additional Radio Frequency Quadrupole Decelerator (RFQD) [11], the ASACUSA

(Atomic Spectroscopy And Collisions Using Slow Antiprotons) collaboration studies the properties of antiprotons and antihydrogen among other experiments.

ASACUSA uses two different approaches to study antimatter, one is the laser spectroscopy of helium atoms that had one electron replaced by a antiproton, so-called antiprotonic helium [12], the other is the direct measurement of the hyperfine splitting of antihydrogen by in-beam microwave spectroscopy [13]. The detector discussed in this thesis is used by the ASACUSA CUSP group in pursuit of the latter. The method chosen by the group closely resembles the experiment by Rabi [14] and shall be discussed further in chapter 3, along with the actual beam line.

1.1. Motivation

As stated above, probing the CPT -invariance is a direct test of the standard model. The results of such a test would either further verify the standard model or hint at new physics beyond the standard model, and could provide insight into the matter-antimatter asymmetry observed in the universe.

The ASACUSA CUSP experiment's method is suitable for an investigation of physics beyond the standard model in the shape of the Standard Model Extension (SME) by Colladay and Kostelecky [15] (see also section 2.2). The SME includes CPT -violating terms in the Lagrangian that would ultimately result in a slightly different hyperfine splitting than in regular hydrogen.

ASACUSA's method is supposed to be very accurate (a precision of $2.7e - 9$ was archived with the same setup using hydrogen [16]), however, there are certain pitfalls. Being located in a experimental hall that houses five other experiments and two accelerators, the ASACUSA beam area is naturally a very noisy place, e.g. there is a multitude of stray fields and unwanted particles. In addition, the laboratory is not underground, so showers of cosmic particles happen constantly. So far the data available for the discrimination of such background events were position and energy information of the central detector, tracks in the hodoscope, time of flight information and a very coarse position information in beam direction. Since this gives only very coarse information about the pion tracks in the beam direction, tracking and vertex reconstruction can effectively only be done in two dimensions [17, 18].

The main goal of this thesis is the implementation of a scintillating fibre detector to provide additional information for three dimensional tracking and background suppression. For this, the detector itself has to be designed, built and integrated into the data acquisition software that is already in place for the other detectors.

2. Physics Fundamentals

This chapter shall give a brief overview of the theoretical and experimental basics associated with the ASACUSA spectroscopy experiment. The section 2.2 provides arguments for a difference in the hyperfine spectrum of hydrogen and antihydrogen.

2.1. The Hyperfine Structure of (Anti-)Hydrogen

The fine structure energy levels in atoms are further split due to the interactions of the magnetic moment of the nucleus with the electromagnetic field of the electron hull. For hydrogen, assuming the ground state, the Hamiltonian for the hyperfine structure can be written as:

$$\mathcal{H} = Ag\hat{\mathbf{I}}\hat{\mathbf{J}} + \hat{\boldsymbol{\mu}}\mathbf{B} \quad (2.1)$$

with A the zero field hyperfine splitting constant, g the gyromagnetic factor, $\hat{\mathbf{I}}$ the nuclear spin operator, $\hat{\mathbf{J}}$ the total angular momentum operator of the electron, $\hat{\boldsymbol{\mu}}$ the operator of the magnetic moment of the nucleus, and \mathbf{B} an external magnetic field.

For $|\mathbf{B}| = 0$, this is reduced to a term only dependant on the nuclear and total angular momentum. Similar to the angular momentum and spin of the electron combining into $\hat{\mathbf{J}}$, an operator for the total atomic angular momentum $\hat{\mathbf{F}} = \hat{\mathbf{I}} + \hat{\mathbf{J}}$ can be introduced. The eigenvalues for $\hat{\mathbf{F}}$ are $F = I \pm J$ and the associated magnetic quantum number that denotes the projection of $\hat{\mathbf{F}}$ onto the magnetic field axis is called M . For the ground state, we get solutions for $F = 0$ and $F = 1$, whereas the $F = 1$ state is triple degenerate with $M = (-1, 0, +1)$. The energy splitting between these two levels is $\Delta E = Ag = h\nu_{\text{HF}}$, with h the Planck constant and ν_{HF} the frequency of the hyperfine transition. This transition frequency is very well known and has been measured as [16, 19–21]:

$$\nu_{\text{HF}} = 1420405751.766 \pm 0.002 \text{ Hz} \quad (2.2)$$

If an external field is present, this degeneracy is resolved, and the $F = 1$ level splits again into three separate components, this is visualised in the Breit-Rabi diagram (fig. 2.2). In an inhomogeneous external magnetic field, these four new states behave differently and can be grouped into two categories corresponding to their behaviour: low field seeking (LFS) states move towards lower magnetic field strengths, high field seeking (HFS) states move towards high magnetic field strengths.

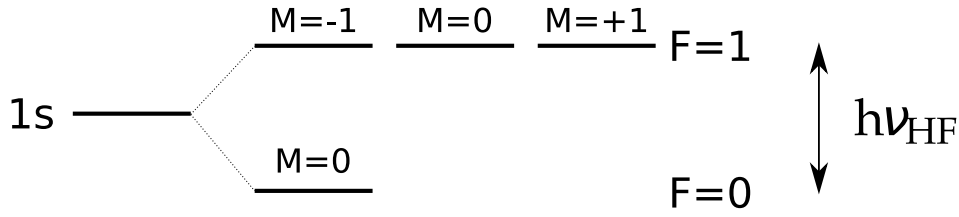


Figure 2.1.: A schematic drawing of the energy levels in (anti)hydrogen due to the hyperfine splitting.

The energy difference of states is $\Delta E = -\hat{\mu}\hat{\mathbf{B}}$. So if states are HFS or LFS is defined by the orientation of the magnetic moment for that particular state relative to the external field. For antihydrogen, $(F, M) = (1, -1), (1, 0)$ have an antiparallel magnetic moment and are therefore LFS and $(F, M) = (1, 1), (0, 0)$ have a parallel magnetic moment and are HFS. For the corresponding states in hydrogen, this is exactly opposite, so $(1, -1), (1, 0)$ are HFS and $(1, 1), (0, 0)$ are LFS.

2.2. Minimal Standard Model Extension

Without any CPT violation, the hyperfine structure is as described above. However, were there CPT -violating terms the degeneracy of the $F = 1$ state in the zero-field case could be lifted. A theoretical framework for such terms beyond the standard model is the Minimal Standard Model Extension (mSME) [23].

The mSME adds CPT and Lorentz-invariance violating terms to the Dirac Hamiltonian in the Dirac equation for hydrogen:

$$(i\gamma^\mu D_\mu - m_e - a_\mu^e \gamma^\mu - b_\mu^e \gamma_5 \gamma^\mu - \frac{1}{2} H_{\mu\nu}^e \sigma^{\mu\nu} + ic_{\mu\nu}^e \gamma^\mu D^\nu + id_{\mu\nu}^e \gamma_5 \gamma^\mu D^\nu) \psi = 0 \quad (2.3)$$

with $iD_\mu = i\partial_\mu - aA_\mu$ the covariant derivative, ψ a Dirac spinor, m_e the electron mass, and assuming natural units $\hbar = c = 1$. The first two additional constants, a_μ^e and b_μ^e are CPT and Lorentz-invariance violating, the others only violate Lorentz-invariance.

These additional terms act like an additional magnetic field, which has several consequences: The energy difference between the two hyperfine states gets altered proportional to the value of the mSME constants. Depending on the extent of the energy shift, the degeneracy of the $F = 1$ state in the zero field region can be lifted, so that there are separated states for $M = -1$, $M = 0$, and $M = 0$.

The energy shift can be determined by measuring and comparing the frequencies of the hyperfine transition for hydrogen and antihydrogen, the lift of the degeneracy can be determined by measuring the transitions at two different external fields and then extrapolating to the zero field.

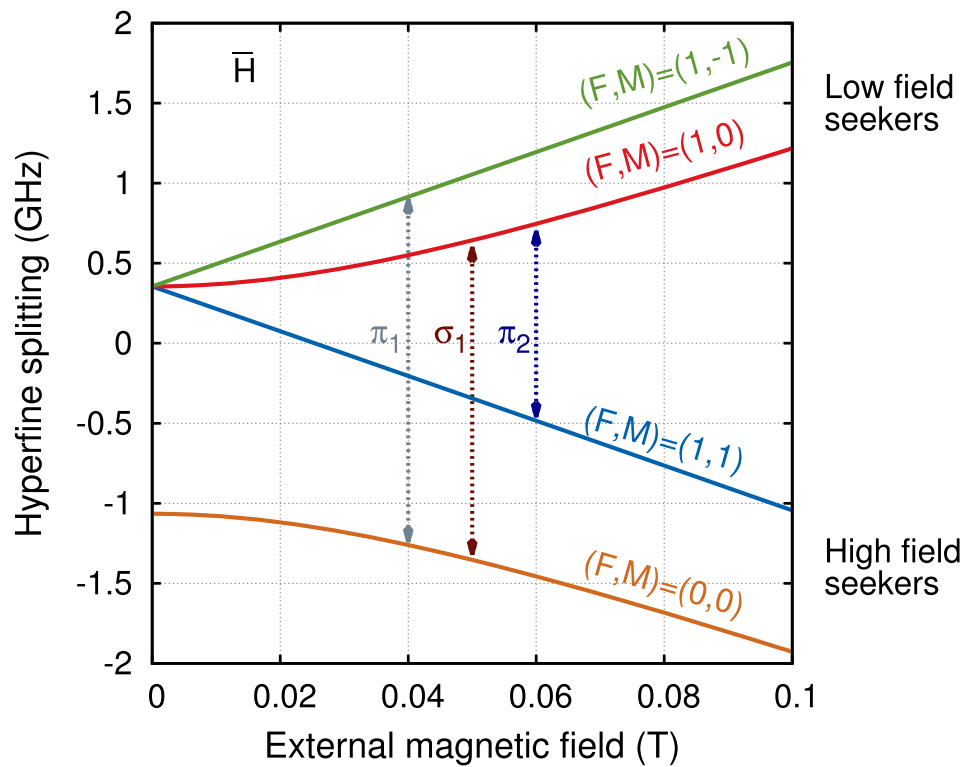


Figure 2.2.: A Breit-Rabi diagram for the ground state hyperfine splitting of antihydrogen. On the right side the classification into HFS and LFS is shown [22].

If there is a CPT -violation as predicted within the mSME framework, the level shifts of hydrogen and antihydrogen could also show differences.

2.3. Antihydrogen Annihilation

Antimatter and regular matter interact in annihilation reactions where both particles are destroyed. Point-like particles like positrons and electrons or quarks and antiquarks react with each other by releasing their combined energy according to the momentum-energy relation $E^2 = p^2c^2 + m^2c^4$ as photons. Hadrons like the nucleons, on the other hand consist of multiple valence-quarks, gluons and sea-quarks. Their annihilations lead not only to the release of photons, but also to the production of bound states of two quarks or antiquarks with opposite colour charges, the mesons.

For antiproton-proton annihilation, the main products are charged and uncharged pions and in some rarer decay channels kaons. The ratios have been experimentally determined, a summary of such measurements for slow antiprotons can be found in M. Hori et. al [24] (2.1). The outcome of antihydrogen-proton annihilations is the same since the only additional particle is a positron. In the case of a antihydrogen-hydrogen annihilation, the positron and the electron would annihilate into photons.

Table 2.1.: Branching ratios for $p + \bar{p}$ reactions. Only the highest fractions are shown. Branches without charged particles are omitted since they cannot be observed with the detector setup described in this thesis. From [24].

Products	ratio
$\pi^+ + \pi^- + 3\pi^0$	23.3 ± 3.0
$2\pi^+ + 2\pi^- + \pi^0$	19.6 ± 0.7
$2\pi^+ + 2\pi^- + 2\pi^0$	16.6 ± 1
$\pi^+ + \pi^- + 2\pi^0$	9.3 ± 3.0
$2\pi^+ + 2\pi^-$	6.9 ± 0.6
$\pi^+ + \pi^- + \pi^0$	5.82 ± 0.43
$2\pi^+ + 2\pi^- + 3\pi^0$	4.2 ± 1
$\pi^+ + \pi^- + 4\pi^0$	2.8 ± 0.7
$3\pi^+ + 3\pi^-$	2.1 ± 0.25
$3\pi^+ + 3\pi^- + \pi^0$	1.85 ± 0.15

2.4. Plastic scintillators

Modern particle and nuclear physics often utilise scintillating materials for the detection of ions and charged subatomic particles. A scintillator emits photons when hit by

certain kinds of particles, whereas different scintillator materials are sensitive for different particles. One of the most common scintillator material is the organic or plastic scintillator made of a polymere, like polystyrene (PS) or polyvinyl toluene (PVT) that has been doped with aromatic compounds called fluors. The polymers are flourescent on their own, however, the light emitted gets reabsorbed within less than 10 mm. If a fluor is present in a concentration of about 1% by weight, a non-radiative energy transfer between two molecules, a so-called Forster transfer, between the polymere and the fluor takes place. Afterwards the fluor in turn emits light in a different wavelength, typically 350 nm to 400 nm, which is able to penetrate the material further by about a factor of 10. For longer scintillators such as scintillating fibres, there is commonly another fluor added in a smaller percentage (0.1% – 0.01%) for the purpose of shifting the wavelength of the emitted light, typically to values of about 400 nm to 500 nm. These wavelengths are already well in the blue part of the optical spectrum, so the light can easily travel through the material further and be picked up by photodetectors [25, 26, p. 416ff].

3. Experimental Setup

This chapter outlines the method used, the beam line and experimental facilities at CERN, as well as the status of the detector up until this thesis. At the end there is a section discussing the hardships in the data analysis that the new detector component is meant to eliminate. The discussion of the old detector version was done in preceding works, such as [27] and [28], and therefore shall be limited to the details necessary for comprehending the changes made for the new detector version.

3.1. Rabi Method

A Rabi-like method for the measurement of hyperfine transitions uses an atomic hydrogen beam and has three major components.

Firstly, the hydrogen beam gets spin-polarised by selecting one spin-state with a strong inhomogeneous magnetic field like in a Stern-Gerlach-like apparatus. The unselected component is removed from the beam with an aperture.

Secondly, the remainder of the beam enters a resonator with an oscillating magnetic field. If the frequency of the field is right, it drives a spin-flip.

Thirdly, the beam, that now contains different states again, is analysed by a second Stern-Gerlach-type apparatus to split the two components again. The separated component can then be detected. By tuning the frequency of the resonator, a measurement of count rate vs. frequency can be done. The closer the frequency gets to the frequency of a transition in the hydrogen atom, the higher the intensity of the flipped component and the lower the intensity of the non-flipped component becomes. In this way, a resonance curve can be observed and the transition frequency be determined from it [14].

ASACUSA uses a method adapted from that for the use with antihydrogen [29, 30]. A crucial difference is that antihydrogen annihilates with regular matter, so only two of the four states can be measured. The remainder also causes some background in the form of annihilations along the beam line. The beam line itself has to be kept in ultra-high vacuum (UHV) in order to keep lifetime of the antihydrogen and antiprotons high enough to traverse the entire beam line.

3.2. Beam line

3.2.1. Accelerator complex

The ASACUSA experiment and so also the detector and accompanying electronics are located at the AD at the CERN facility near Geneva. The AD is part of the Proton Synchrotron complex (PS complex), that also encompasses a few other, mostly fixed-target experiments, and acts as a pre-accelerator for the Super Proton Synchrotron (SPS) and the Large Hadron Collider (LHC, see also fig. 3.1).

By injecting the PS proton beam into a very dense target material, such as iridium or tungsten, antiprotons are produced. These are collected electromagnetically and injected into the AD. The AD uses a cycle of three deceleration steps and three cooling steps. Deceleration is facilitated by using radio frequency (RF) cavities, the antiproton beam is cooled via stochastic cooling and electron cooling [32]. Figure 3.2 shows the AD cycle with all deceleration and cooling steps.

After the beam reaches the target energy of 5.3 MeV, it is ejected from the ring and injected into the experimental areas, located at beam height within the perimeter of the ring. In ASACUSA's case, the beam is injected into the RFQD. It decelerates around 30% – 40% of the beam further to a target energy of about 100 keV [11]. The remaining, un-decelerated component of the beam also enters the beam line and, as the trapping system is not tuned to its energy, hits a wall or gate valve and annihilates. This causes a shower of annihilation products in the experimental area that has to be considered in the design of the trigger system.

3.2.2. Antihydrogen Source

After the RFQD the decelerated beam reaches ASACUSA's catching trap, MUSASHI (Monoenergetic Ultra Slow Antiproton Source for High-precision Investigations), a Penning-Malmberg-type trap featuring a homogeneous magnetic field and multi-ring electrodes (MRE). MUSASHI catches the beam, cools it with electrons and applies the rotating wall technique to compress it [33]. After the electrons used for cooling are ejected from the plasma, it is extracted and transferred downstream into the mixing trap. The mixing trap (named CUSP trap after the magnetic field shape) also consists of MRE and a superconducting magnet, however, the magnet is built in a double anti-Helmholtz configuration, resulting in a field that diverges at two locations. Whilst additional challenges for the confinement of antiprotons are posed by the diverging magnetic field, the advantage over other configurations is that the antihydrogen gets spin-polarised in the process, eliminating the need for a separate polariser [34].

3. Experimental Setup

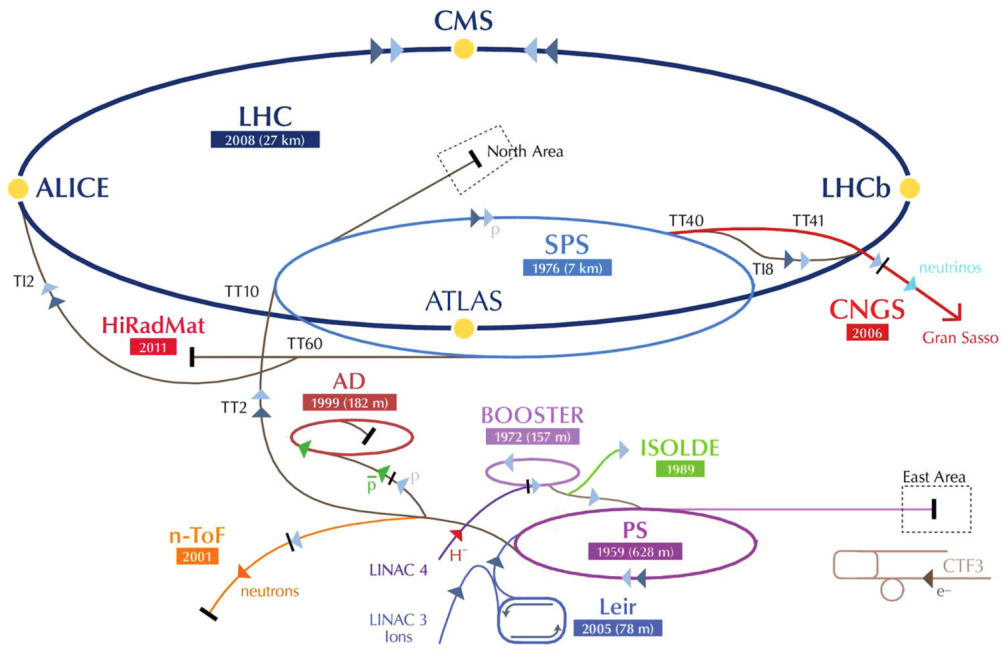


Figure 3.1.: The CERN accelerator complex [31].

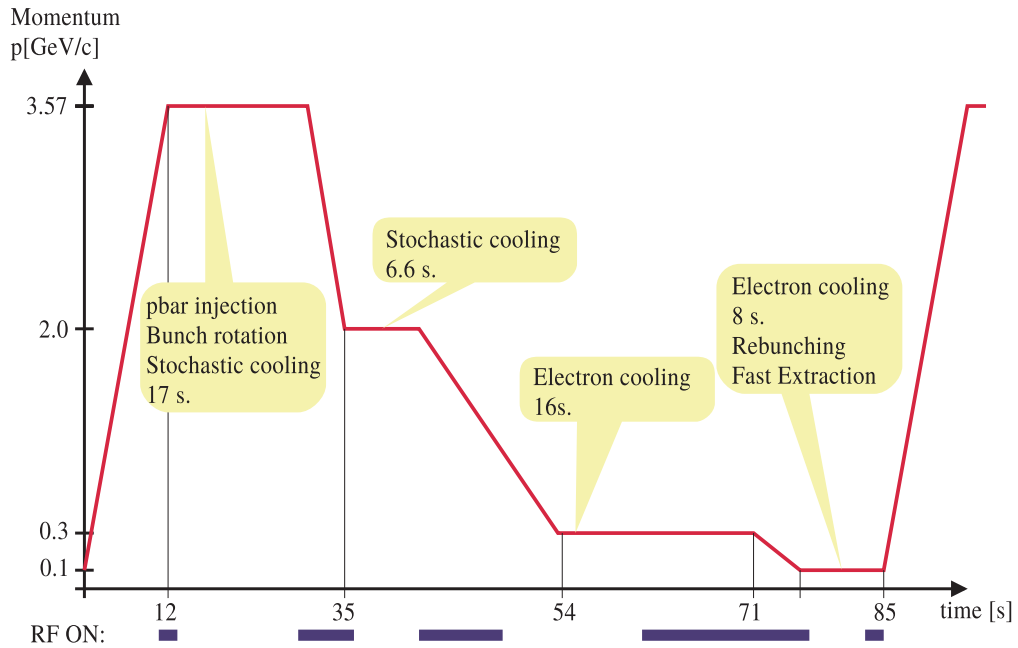


Figure 3.2.: The deceleration cycle of the Antiproton Decelerator [32]. In 2016 and 2017, the cycle is around 108 s long, due to a pause in between ejection and injection from and into the AD ring. However the length of this pause varies sometimes.

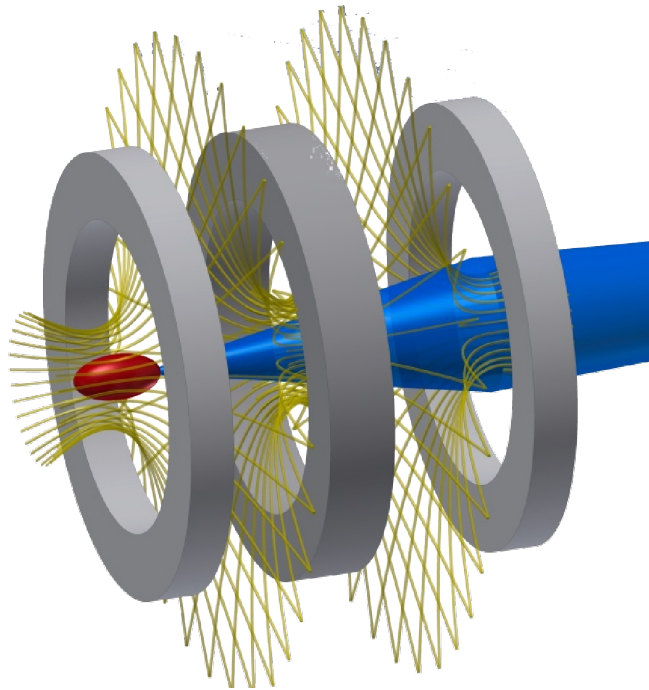


Figure 3.3.: An artistic representation of the double cusp field in the CUSP trap. Yellow are the magnetic field lines, red is the interaction zone, and blue is the beam of antihydrogen. Render by D. Pristauz-Telsnigg.

For antihydrogen synthesis positrons are also required. The positrons stem from a ^{22}Na source, where they are produced in a β^+ -decay:



After production, they are moderated by a solid neon moderator and accumulated in another Penning-Malmberg-type trap with a buffer gas cell containing nitrogen before being transported to the CUSP trap.

For antihydrogen production, the antiprotons and positrons are confined in a Penning-Malmberg-type trapping potential within the CUSP trap. The recombination to antihydrogen can then be facilitated using different methods, such as the direct injection [35].

During a antihydrogen synthesis cycle, the freshly formed antihydrogen atoms are electrically neutral and can therefore exit the trap in the production region. If the trapped antiprotons were static, the directions of the momenta of the antihydrogen atoms would be distributed evenly and they would exit the production region isotropically. However due to the rotational motion of the antiproton plasma, the antihydrogen could have an increased momentum in radial direction, making the process anisotropic. Of course only a certain amount leaves the trap in direction of the antihydrogen detector. To be able to do diagnosis and measurements within the CUSP, it is also fitted with the ASACUSA Micromegas Tracker (AMT). This detector takes the form of a half cylinder surrounding the CUSP MRE on the lower half. It is made from two layers of Micromegas (MICRO MESH Gaseous Structure) detectors and one plastic scintillator in between. The plastic scintillator is read out by multiple photo multiplier tubes connected to the ends of the half-cylinder via light guides. The AMT is used to measure annihilations within the trap during the antihydrogen formation cycle [36].

The antihydrogen is either magnetically high-field-seeking (HFS) or low-field-seeking (LFS). The fractions for both HFS and LFS antihydrogen in the ASACUSA setup can be determined by Monte Carlo simulations and analytical calculations, such as found in Y. Nagata and Y. Yamazaki [34]. The magnetic field of the CUSP defocuses antihydrogen atoms in HFS states and only the antihydrogen in LFS states is focused toward the beam axis and travels further down the beam line. At the downstream side of the CUSP, the electrodes are used to create the so called Field Ionizer Trap (FIT) a region with an electric field strong enough to re-ionise antihydrogen atoms with a principal quantum number higher than $n = 39$ (see also fig. 3.4). The potential also reflects uncaptured antiprotons, so that particles measured by the AMT and AMT scintillator detectors in the FIT region stem most likely from antihydrogen. Furthermore, antiprotons from re-ionised antihydrogen in higher n states get captured in the FIT potential well and can be extracted and measured to get an estimation of the number of antihydrogen produced in higher n states.

3. Experimental Setup

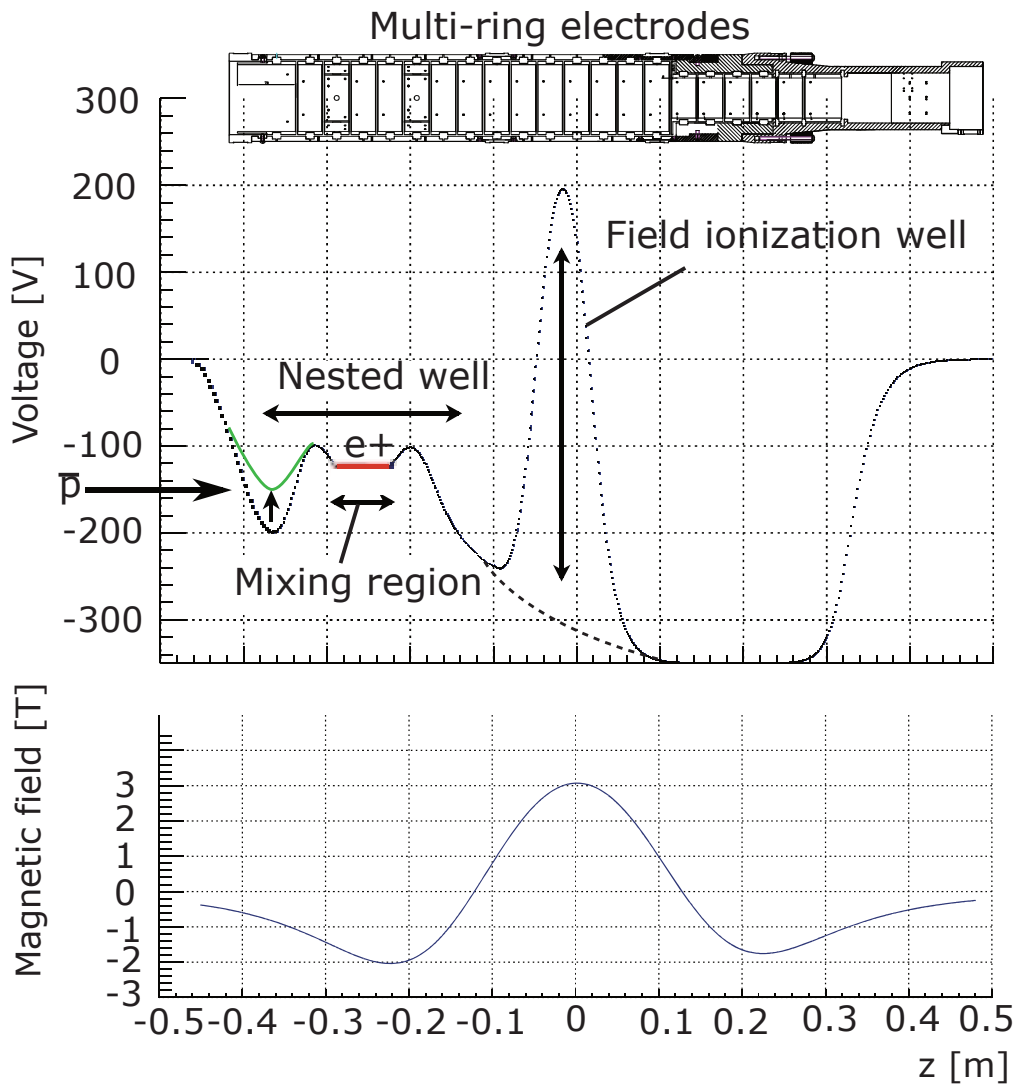


Figure 3.4.: From the top: Drawing of the CUSP MRE, electric trap potential and magnetic field. The trap potential shown is used in the direct injection mixing scheme [37].

Assuming a velocity of $1000 \frac{\text{m}}{\text{s}}$, antihydrogen atoms with a principal quantum number of $n = 12$ should de-excite to the ground state during the time needed to traverse the spectroscopy apparatus, so a stronger re-ionisation is necessary. For this task, a so-called field ioniser (FI) is mounted after the CUSP trap. It employs two mesh-electrodes that add as little material as possible in the flight path of the antihydrogen whilst creating an electric field strong enough to dissociate antihydrogen in quantum states higher than $n = 12$ (around $20 \frac{\text{kV}}{\text{cm}}$) [35]. One important point is that there is a beam component directly upon the beam axis, on which both the polarising and analysing magnetic fields cannot act as the B -field along the axis is 0. To remove this component, the FI chamber is fitted with a beam blocker that can be pneumatically moved into the beam. This is an active beam blocker comprising a small passivated implanted planar silicon (PIPS) detector that can be used as a normalisation counter [38].

3.2.3. Spectroscopy apparatus

The spectroscopy beam line connected to the CUSP trap comprises of a microwave cavity and a superconducting sextupole magnet. The cavity is a strip-line microwave cavity surrounded by McKeehan-coils. The coils provide a homogeneous magnetic field, while 1.42 GHz microwaves corresponding to the hyperfine transition frequency ν_{HF} are coupled into the cavity to induce spin-flips. The maximum de-tuning of the cavity allows for a frequency scan of two transitions between HFS and LFS states, σ_1 and π_1 [39]. Depending on the orientation of the homogeneous field in relation to the oscillating field, one of the two transitions can be selected. For this, the coils can be turned around the cavity. A more thorough description can be found in the PhD thesis of S. Federmann [39].

The sextupole magnet acts as the analyser in the beam line, it defocuses the antihydrogen atoms that performed a spin-flip into an HFS state in the cavity. Since for the spectroscopy it is advantageous to have a large acceptance, the analysing magnet was designed to be super-conducting, so it can create sufficient field gradients in a 100 mm beam pipe. For the 2017 beam time however, the main goal was to optimise the antihydrogen production, so the detector was mounted right after the FI chamber.

For an overview of the beam line, refer to figure 3.5 and figure 3.6.

3.3. Detector

The antihydrogen detector consists of a two layered hodoscope (see fig. 3.7) and a central $\text{Bi}_4\text{Ge}_3\text{O}_{12}$ (BGO) crystal scintillator [27, 28, 40]. The hodoscope is a barrel-type detector with an octagonal cross section that covers a solid angle of approximately 80% of the total solid angle (4π) seen from the central detector. Each side is composed of four bars of the plastic scintillator material EJ-200 [41]. In total, the two layers consist

3. Experimental Setup

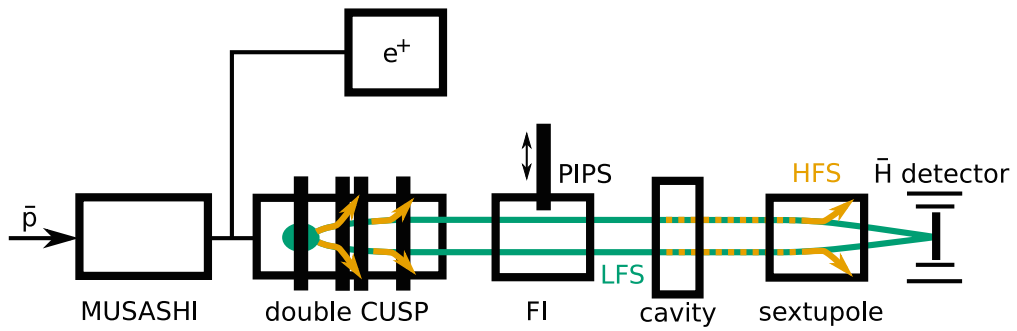


Figure 3.5.: A schematic drawing of the beam line. Orange are HFS antihydrogen atoms, green LFS antihydrogen atoms [38]

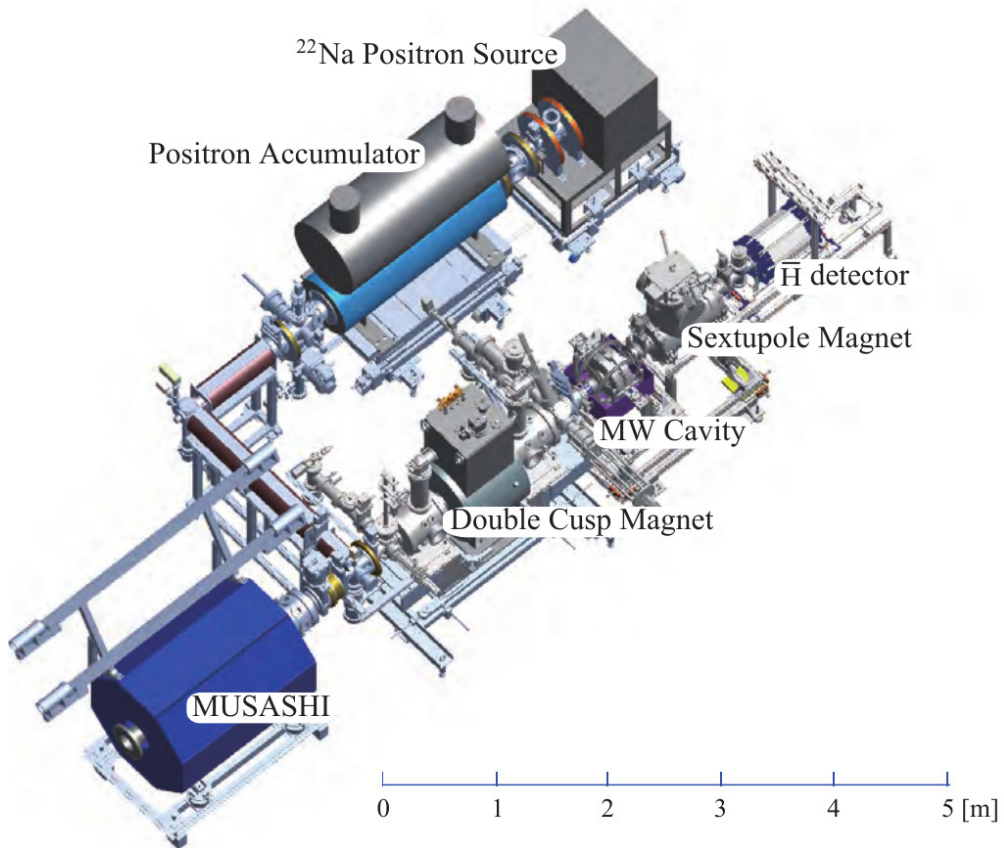


Figure 3.6.: A rendering of the full beam line with all components marked. Render by N. Kuroda.

of 32 bars each, whereas the outer bars are 35 mm wide and 450 mm long, the inner bars 20 mm wide and 300 mm long (see fig. 3.7). The thickness of the bars is identical in both layers and amounts to 5 mm. On both ends of each bar plastic light guides and two serially connected Ketek PM3350TS silicon photo multipliers (SiPMs) are glued on [27, 28, 41]. SiPMs are arrays of avalanche photo diodes. Each individual cell is a diode biased in the reverse direction near the breakdown voltage. Incoming photons create charge carriers via the photo-electric effect, which in turn causes a measurable pulse if enough cells are triggered. In total there are 128 output channels on the hodoscope once fully assembled, one per end of each bar [27, 28]. The signal of each channel is pre-amplified and pre-processed by electronics adjacent to the detector and then fed into the main data acquisition system outside the beam area (see sec. 5).

Within the hodoscope, a vacuum chamber made from a CF-100 beam pipe containing the BGO detector is situated. The BGO disc is coupled to four multi anode photo multiplier tubes (MAPMTs). Whilst the BGO is inside the vacuum chamber, the MAPMTs reside outside at normal pressure. They are optically coupled to each other through a borosilicate glass window. The MAPMTs record the scintillation light from the BGO with 8-by-8 pixels each, resulting in a 16-by-16 pixel square that covers the whole BGO disc with a slight distance in between the sensitive area of each MAPMT. The signals from the MAPMTs are amplified by Clear Pulse 80190 photo multiplier amplifiers attached to the MAPMTs and then sent to the Clear Pulse 80057 data recorder in the main data acquisition (see also sec. 5).

A more thorough discussion of the old detector setup can be found in [27] and [28].

3.4. Detection of Antihydrogen Annihilation Events

In the existing antihydrogen detector, the recorded data provides information about the location of the annihilation on the BGO disk, the energy deposited there and which scintillator bars in the hodoscope were hit. In principle, a position resolved read out of the scintillator bars is possible by comparing the signal amplitudes and the time of arrival of the signals for both ends of the scintillator bar. However, practically this requires an order of precision that is not trivial to facilitate in a harsh environment such as an experimental hall. So far only a longitudinal resolution of around 7 cm has been achieved this way [17, 18]. This can be used to discriminate against random coincidences between the upstream and downstream SiPMs, since they produce longitudinal positions outside the hodoscope, as well as cosmic particles. However, the resolution is not sufficient for three-dimensional tracking and vertex reconstruction.

By calculating additional information from the data, such as angles of tracks relative to each other or the time-of-flight through the detector, the two-dimensional analysis can be quite successful. Nevertheless, a fully three-dimensional tracking and vertex reconstruction would increase the cosmic rejection further while decreasing the likelihood of

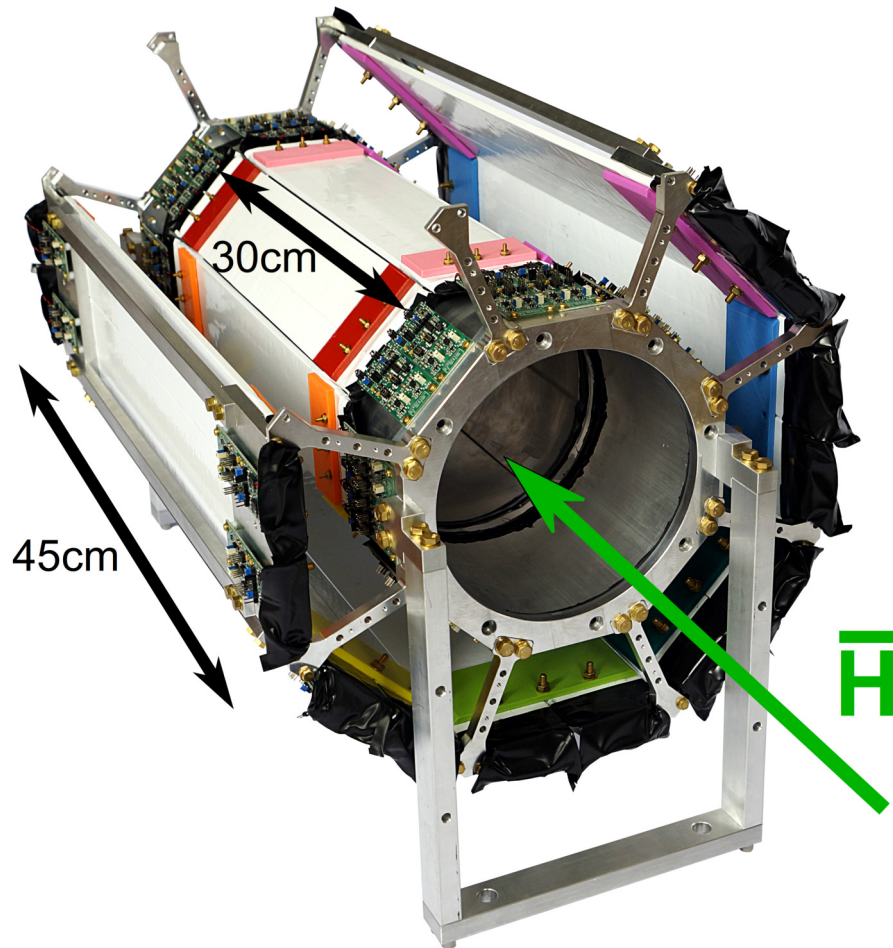


Figure 3.7.: The hodoscope with dimensions marked. The green arrow symbolises a beam of antihydrogen during an experiment.

real events being misidentified as background. Considering the low statistics, it is of utmost importance to improve the identification rate as much as possible.

The following two sections show possible types of events that can be reduced in or completely removed from the dataset by employing 3D vertex reconstruction.

3.4.1. Experimental Background

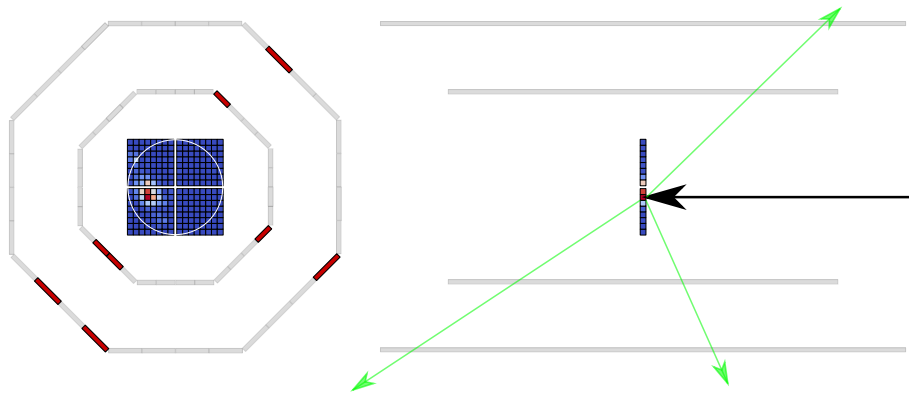
A big problem that cannot be solved with 2D analysis alone are signals stemming from annihilations of defocused HFS antihydrogen and over- or under-focused LFS antihydrogen annihilating in the vicinity of the BGO or on the walls. Especially events in the second category often happen close to the BGO within the solid angle seen by the hodoscope (see fig. 3.8b). Such an event can easily trigger the system since the outcome in terms of particles is the same, and distinguishing it from others is difficult.

3.4.2. Cosmic Background

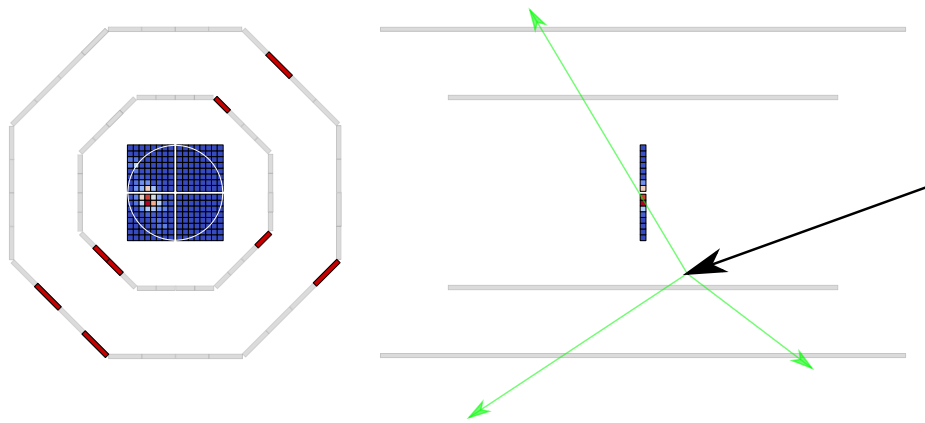
Since the AD facility is not underground like many other accelerator installations, the incidence of cosmic particles with an approximately constant rate is to be expected. Charged cosmic particles passing through the detector cause scintillation light and deposit some energy in the BGO, so they can trigger the system. Most cosmics can be filtered out by using the time-of-flight of their traversal through the detector, or by the fact that cosmics usually travel in straight lines due to their high energy. However, if a cosmic particle is scattered or produces a shower of secondary particles, the characterisation of such events is difficult.

Examples for events are shown in figure 3.8.

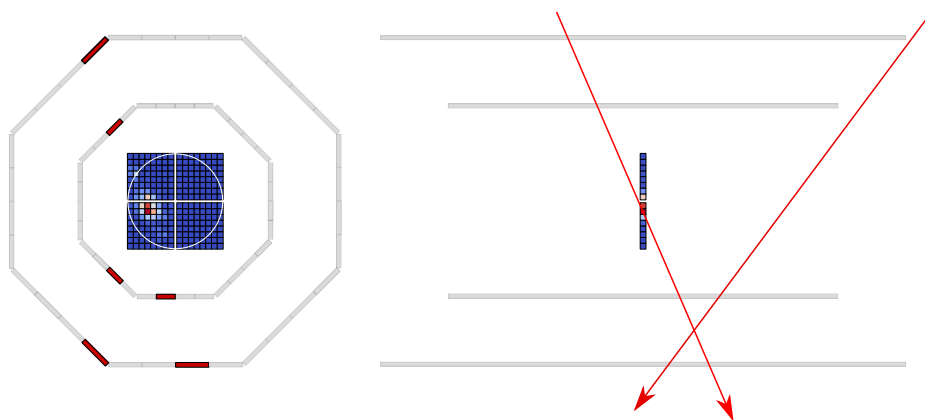
3. Experimental Setup



(a) A regular event. The 2D image shows the hit in the center and three tracks.



(b) Antihydrogen annihilating on the wall of the beam pipe. The three pions trigger the system and produce a signature similar to a real event.



(c) A cosmic event. Despite being caused by cosmic alone, the signature looks very similar to an antihydrogen event.

Figure 3.8.: Examples for events that cannot be completely distinguished with two-dimensional analysis. Black is the impinging antihydrogen, green are pions from the annihilation and red are cosmic particles. The left hand side is the situation as seen in beam direction, the right hand side shows a perpendicular view.

4. The Hodoscope Fibre Detector

In this chapter an in-depth description of the fibre detector added to the existing hodoscope shall be given. Covered are the design phase, test measurements using prototypes, as well as the final assembly.

4.1. Concept and Design

The goal of the fibre detector is to solve the problems in the data analysis mentioned in section 3.4, so the design guideline was a fibre-based detector that provides a longitudinal resolution in the order of mm.

The final design consists of two layers made of fibres. In each layer the fibres do one turn each and cover the whole circumference tightly. The readout is situated on one end of the fibres only. The fibres are wound on two tubes, one for the inner layer, one for the outer layer to support them and keep them in shape. These tubes are both manufactured from carbon to reduce the probability of particles scattering in the support structure as well as to keep the overall structure as light as possible. Their dimensions were chosen so that the distance between the two layers is maximised whilst keeping the shape of the bar hodoscope. The exact sizes can be found in table 4.1. The tube for the inner layer also replaces an aluminium tube that made up the inner support structure of the bar hodoscope.

Table 4.1.: Dimensions of the carbon tubes supporting the scintillating fibres

	Length [mm]	Inside diameter [mm]	Wall thickness [mm]
Inner tube	270	165	1
Outer tube	420	288	2

For winding the fibres around the tubes, a rectangular cross-section has shown to be beneficial, as round fibres would have had to be either glued or very thin. Round fibres would also leave air gaps, while rectangular fibres can be stacked side by side. Glueing did affect the attenuation negatively, and thinner fibres would have been unfeasible with the SiPMs used. The final choice are square fibres with an edge length of 2 mm, four of which are attached to one SiPM, resulting in a square bundles of 2x2 fibres with an total edge length of 4 mm, which leads to a resolution of approximately 7.72 mm in

the z coordinate on the hodoscope axis. The resolution is estimated with an geometric model (fig. 4.1), averaging the minimum distance of two points on the central axis that can be separated for several different angles of incidence. Also only paths that hit only one fibre bundle per layer are considered.

The end without an SiPM is slightly tucked under the end with an SiPM since there has to be a short, straight section to reduce the stress on the joint with the SiPM (see fig. 4.2). To ensure a uniform coverage, the ends with the SiPMs are shifted by one eighth of a turn in between layers.

As material for the fibres, Saint Gobain BCF-12 was chosen. This material features a emission peak at 435 nm, while the used KETEK PM₃₃₅₀-EB SiPMs have their maximum photo detection efficiency at 430 nm. The full specifications for both can be found in appendix C.1 or in [42, 43]. Noteworthy is that the fibres are clad with acrylic, which makes them resistant against dirt and fingerprints, but reduces the active area by 4%. Furthermore, the cladding also reduces the cross-talk, the transmission of light in between adjacent fibres.

The SiPMs are soldered onto small circuit boards using reflow soldering where a solder paste is applied to the circuit boards, the SiPMs are stuck into the paste, and the whole batch is heated so that the paste becomes liquid for a short time. While liquid, the solder pools around the solder pads of both the part and the circuit board and forms solid solder joints when cooling down. Twisted pair cables for the connection to the preamplifiers are soldered on to additional solder pads on the SiPM circuit boards manually. To fully take advantage of the noise-cancelling effect of twisted pair cables, they have to be twisted as tightly as possible, so a special device was constructed and used for twisting. When finished, the cables have a length of ~ 100 cm.

On both ends each tube has an end ring that is used for mounting to the existing support structure of the hodoscope. The end pieces for the outer layer are made from 3D printed

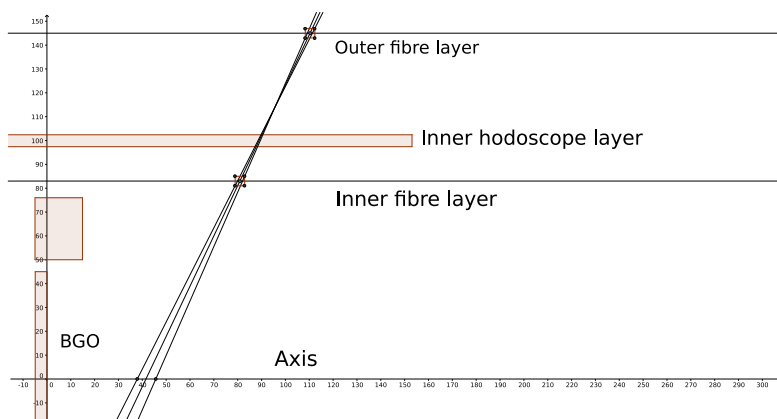


Figure 4.1.: A drawing of the geometric model used for resolution estimation.

4. The Hodoscope Fibre Detector

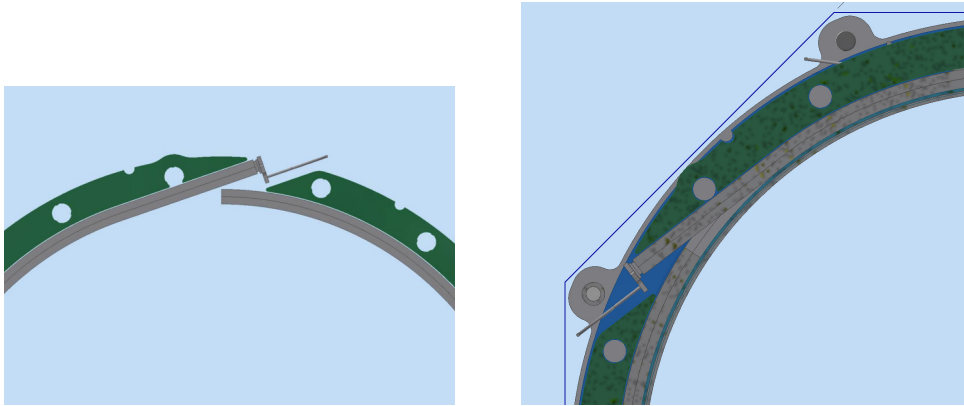


Figure 4.2.: Drawings of the overlapping section of fibre bundles. Drawings by D. Pristauz-Telsnigg.

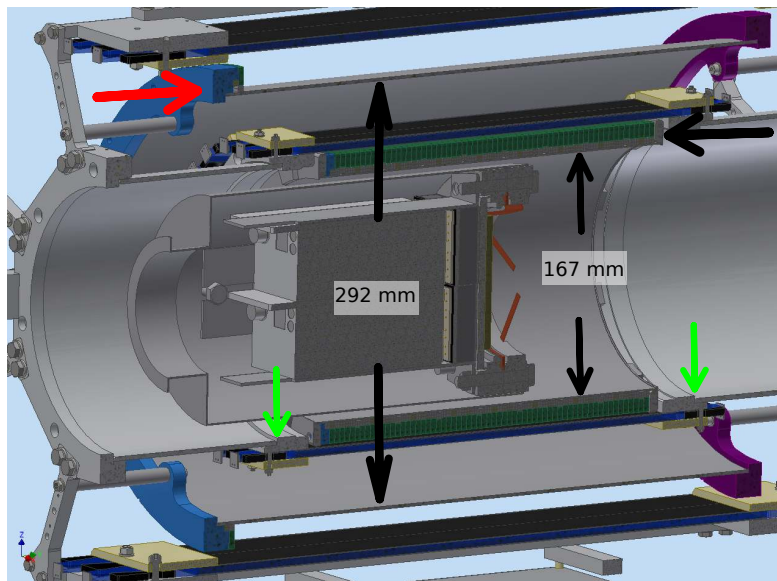


Figure 4.3.: A rendering of the detector including fibres and bars. The black arrows mark the outer diameter of the carbon tubes, the red arrow marks one of the 3D printed end pieces of the outer layer, and the green arrows mark the section where the old support is replaced by the carbon tube of the inner fibre layer. Render by D. Pristauz-Telsnigg.

ABS plastic, while the end pieces for the inner layer are made from aluminium, since it also serves structural purposes.

The fibre bundles are secured in place by plastic rings that are fixed to each other and the end pieces by plastic bolts. These plastic rings are also made from ABS but are laser-cut instead of printed, since this technique allows for a higher production volume while providing narrower error margins on the measurements. 3D printed rings were tested but ultimately rejected as the imprecise edges made the winding of fibres almost impossible.

4.2. Prototype Measurements

In preparation for the assembly several measurements were carried out to resolve open questions. For measurements that required the fibres to be bent in the final shape, models of the detector assembly were 3D printed from ABS plastic.

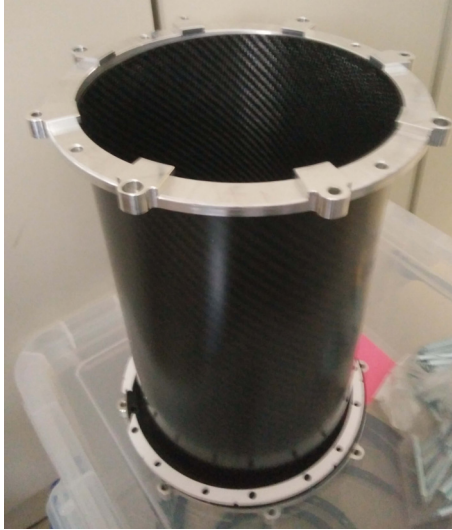
To determine the best treatment of the loose end of the fibres, measurements with differently prepared fibres were made. Four fibre bundles were prepared: cut at the end, cut and painted white, cut and polished, polished and painted white. The bias current is to be adjusted for each bundle separately to get a cosmic count rate of about 0.3 Hz, the values are found in table 4.2. The fibres are wound into a prototype of the outer layer and a ^{90}Sr source is placed on the side. Data are taken with a LeCroy WaveRunner 6 Zi Oscilloscope with two different trigger settings for a duration of 600 s per setting and per fibre. The result can be seen in figure 4.7. For the -100 mV trigger level, all fibres are similar, for -200 mV, the signals in the cut fibres decrease. Painted and polished surfaces create multiple reflections that contribute to the high count rate, while the rough surface of the cut fibre suppresses reflections. Since it is more desirable to have single signals as reflections would only cause noise, all future fibres were cut only.

Table 4.2.: Bias settings for the comparison between different end treatments

Treatment	Bias [μA]
Cut	5.18
Cut and painted	5.21
Polished	5.19
Polished and painted	5.16

Another point of concern is the attenuation in the fibres in the inner layer. Preparatory measurements showed that the attenuation had a dependency on the bend radius. To test this, fibres are wound into a model of the inner layer and the count rate with a ^{90}Sr source is measured for different thresholds. The results can be seen in table 4.3. While

4. The Hodoscope Fibre Detector



(a) The inner carbon tube. At the top and at the bottom the aluminium end pieces can be seen.



(b) The outer carbon tube. The upper end is bare, on the lower end the end piece and a ring used to secure the fibre bundles are mounted.

Figure 4.4.: Pictures of the carbon tubes that make up the support for the fibre bundles.



Figure 4.5.: Detail shot of one of the plastic rings used to secure the fibre bundles in place. The black parts are the plastic bolts used to mount the rings to each other.

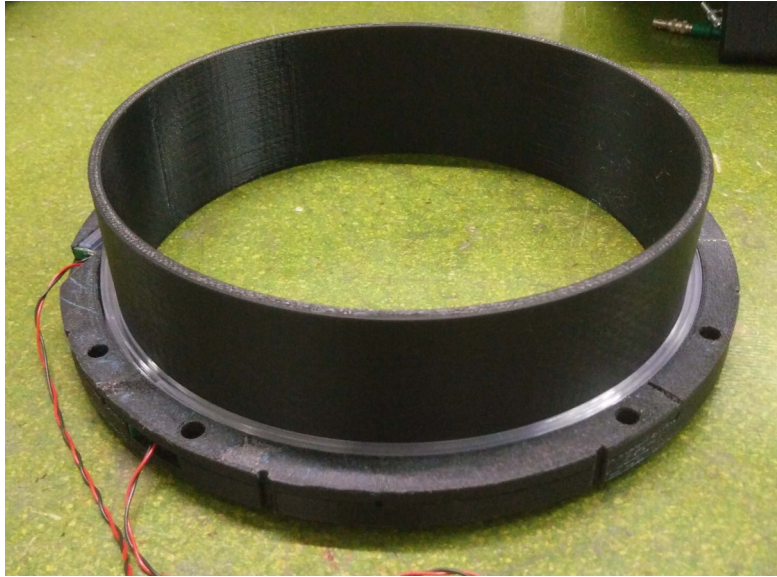


Figure 4.6.: The 3D printed prototype of the inner fibre layer used for measurements.

about $\sim 20\%$ lower than the count rates for straight fibres or the outer layer, the results show that enough light is reaching the SiPMs.

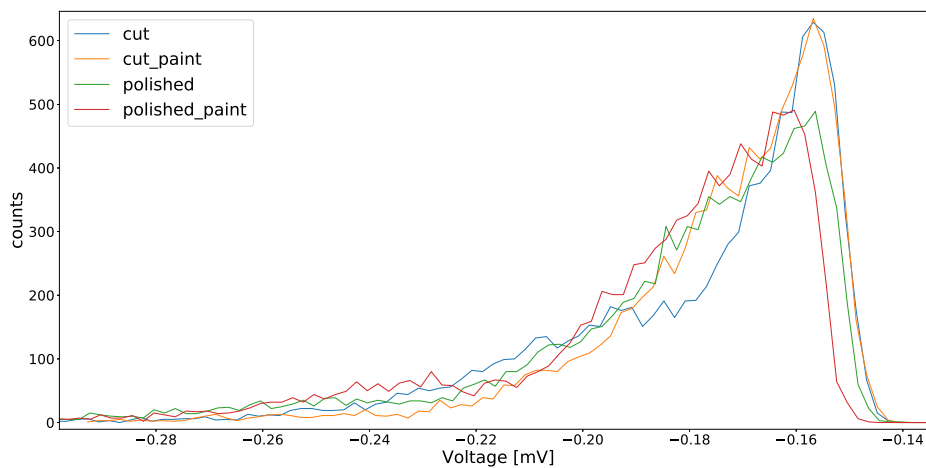
Table 4.3.: Test measurement with a bundle of fibres in a model of the inner layer. Measurement time is 300 s, the bias current is $1.48 \mu\text{A}$

Threshold [mV]	Count rate with source [Hz]	Count rate without source [Hz]
-150	71.13	6.85
-250	65.08	0.64
-350	48.30	0.30
-500	16.56	0.14
-550	9.62	0.12

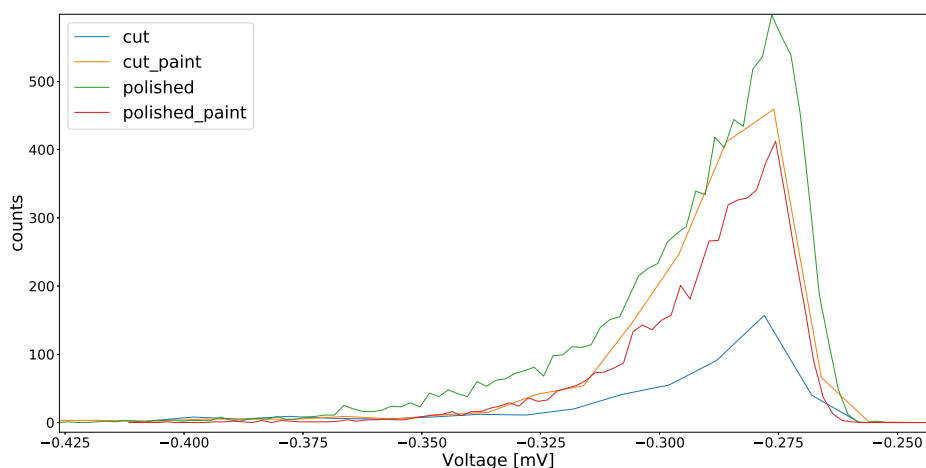
A final measurement was conducted to determine the amount of cross-talk between adjacent bundles of fibres. This is done by winding two fibre bundles into a prototype of the outer layer. The free end of the fibre on top is partially removed from the prototype and secured behind a ~ 3 cm thick Al block. This way, the end of one fibre can be exposed to a β source while more than half of the bundle are still in close proximity to the bottom fibre. The Al block shields the bottom bundle from the source, so any counts in the bottom bundle are either light spilling over from the top bundle or regular background (see fig. 4.8).

As a source ^{90}Sr was used, the threshold was set to -300 mV and the measurement time was 300 s. The bias current was again set by fixing the dark count rate to around

4. The Hodoscope Fibre Detector



(a) Threshold -100 mV



(b) Threshold -200 mV

Figure 4.7.: Histograms of counts under threshold for different end treatments and two different threshold levels with a ^{90}Sr source. The histogram peaks are connected to provide a better visibility. Since the amplification electronics used output a negative signal, the values on the x-axis are negative and the measurement looks at events under the threshold.

3 Hz, and was $1.33 \mu\text{A}$ for the bottom bundle and $4.77 \mu\text{A}$ for the top bundle. According to the results in table 4.4, there is practically no crosstalk.

Table 4.4.: Measurement of the crosstalk between two bundles. Measurement time is 300 s, the bias current is $1.33 \mu\text{A}$ for the bottom bundle and $4.77 \mu\text{A}$ for the top bundle.

Bundle	Count rate with source Hz	Count rate without source Hz
Top	64.04	0.31
Bottom	0.28	0.34
Coincidence	0.03	0.02

After these measurements were finished, the model and a spare fibre bundle were used for DAQ development.

4.3. Assembly

For the final assembly almost 200 fibre bundles had to be glued to their SiPMs. Before glueing, they are cut to the right length and the side where the SiPM is going to be situated was polished to remove any dirt or unevenness. For each layer, two different lengths must be cut, so that the ends of the wound fibres are at the same level. The lengths can be found in table 4.5. Afterwards they are grouped into bundles of four, two shorter and two longer ones, and affixed to each other with a stripe of Kapton tape.

Table 4.5.: Length of the cut fibres. Top and bottom refer to the order of the fibres in on bundle, whereas bottom is the one that is further inside when installed.

Fibre position	Length [mm]
Inner layer, bottom	531
Inner layer, top	544
Outer layer, bottom	924
Outer layer, top	936

As a glueing agent a two-component optical cement called BC-600 from Saint Gobain was used. This is an adhesive specially made for SiPMs and matches the optical properties of the fibres as well as the protective acrylic cover of the SiPM to avoid reflections and scattering. The adhesive has to be mixed in a ratio of 100:28 resin to hardener and solidifies after around 12 hours, however it continues to harden. Since the contact surface of the fibres is quite small, the glue was left to harden for 24 hours after application to ensure safe handling. The components of the glue are stored refrigerated,



Figure 4.8.: Setup for the crosstalk measurements. A 3D printed model of the outer layer is used. The Sr_{90} source is shielded by an aluminium block.

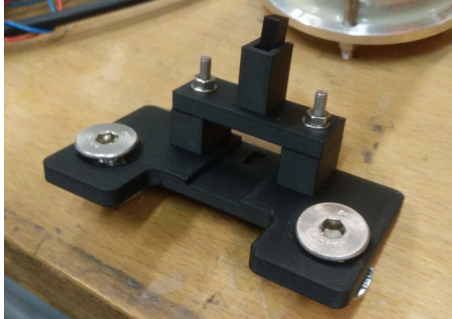
and have to be put into room temperature two to three hours before use to fully warm up.

To simplify and streamline the process, glueing fixtures were 3D printed. They have an indentation supposed for the SiPM and a guide for the fibre bundle that gets inserted from above. Once the bundle is in full contact with the SiPM, it is fixed with a clamp and left to harden.

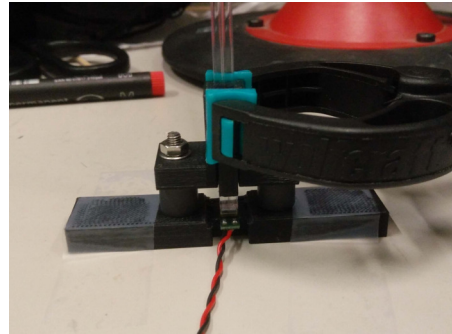
Once the joints are completely hardened, they are wound into the detector. Each bundle is then measured with and without the ^{90}Sr source to determine if it is functioning correctly. Bundles that do not reach a certain count rate are removed and replaced with a new one. The values for the accepted fibres can be found in appendix C.2. When a fibre shows a good count rate, it is secured with a plastic ring and the SiPM's cable is glued on to release tension and protect the solder points. If a bundle is especially unruly, it is additionally fixed in place with Kapton tape. That way the assembly continues until the upper edge of the carbon tube is reached, then the second end piece is glued on.

After the assembly at SMI finished, the detectors were transported to CERN, where they are checked for damages and then light-tightened. To ensure light-tightness, both the inner and outer layer are wrapped in black isolation tape, whereas the stripes are placed in an overlapping manner. Once the wrapping was finished, both layers are covered in black latex paint to seal small gaps in the tape, especially at the edges since they are most exposed to light. During this process the light-tightness is monitored by comparing count rates with and without a black cloth on top of the detector. As

4. The Hodoscope Fibre Detector



(a) The 3D printed guide for glueing the fibre bundles to the SiPMs.



(b) The 3D printed guide for glueing. A fibre bundle is inserted and clamped in place.

Figure 4.9.: Photos of the guide for glueing the fibres.

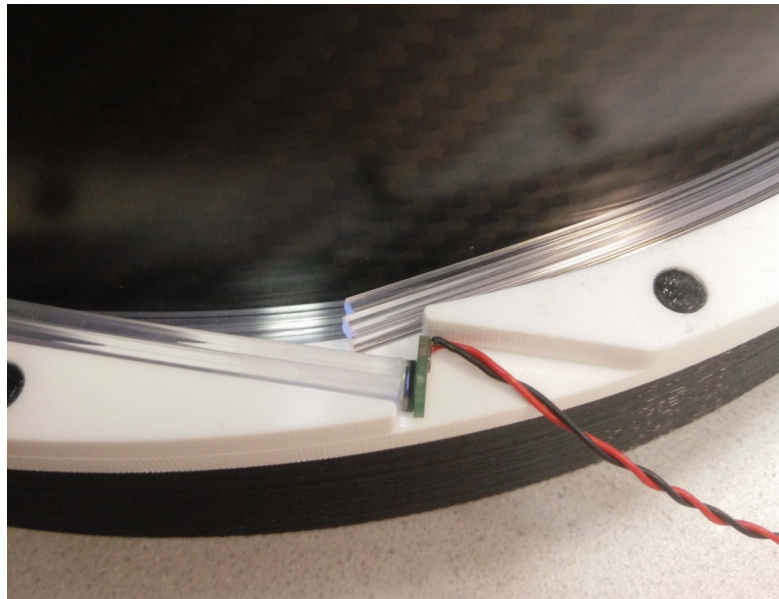
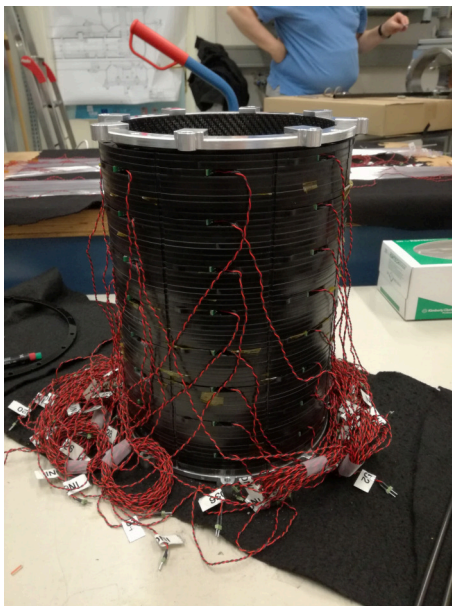


Figure 4.10.: Detail photo of a fibre in place. The securing ring and the overlap section can be seen. The protruding section of the SiPM board is always pointing inward, to avoid damages.

long as there are differences, light-tightness is not achieved and another layer of latex has to be added. When the inner layer is finished, it can be built into the remaining hodoscope support structure and the inner hodoscope bars can be mounted. This has to be done carefully since there might be slight differences in the length between the mounting screws as the inner support was replaced by the inner fibre layer. The outer fibre layer is mounted next and at the end the outer bar layer and the amplifier boards. Afterwards the whole setup can be transported into the beam area.

In addition to the amplifier hardware for the existing hodoscope, eleven additional amplifier boards have to be distributed on the hodoscope itself and on the support structure (see 5.2.4). The cables from the SiPMs are plugged into the boards and the boards into the data acquisition (DAQ) (see chapter 5), a table matching the fibres and the amplifier channels can be found in appendix C.6.



(a)



(b)

Figure 4.11.: The completely wound inner (a) and outer (b) layers.

4. The Hodoscope Fibre Detector

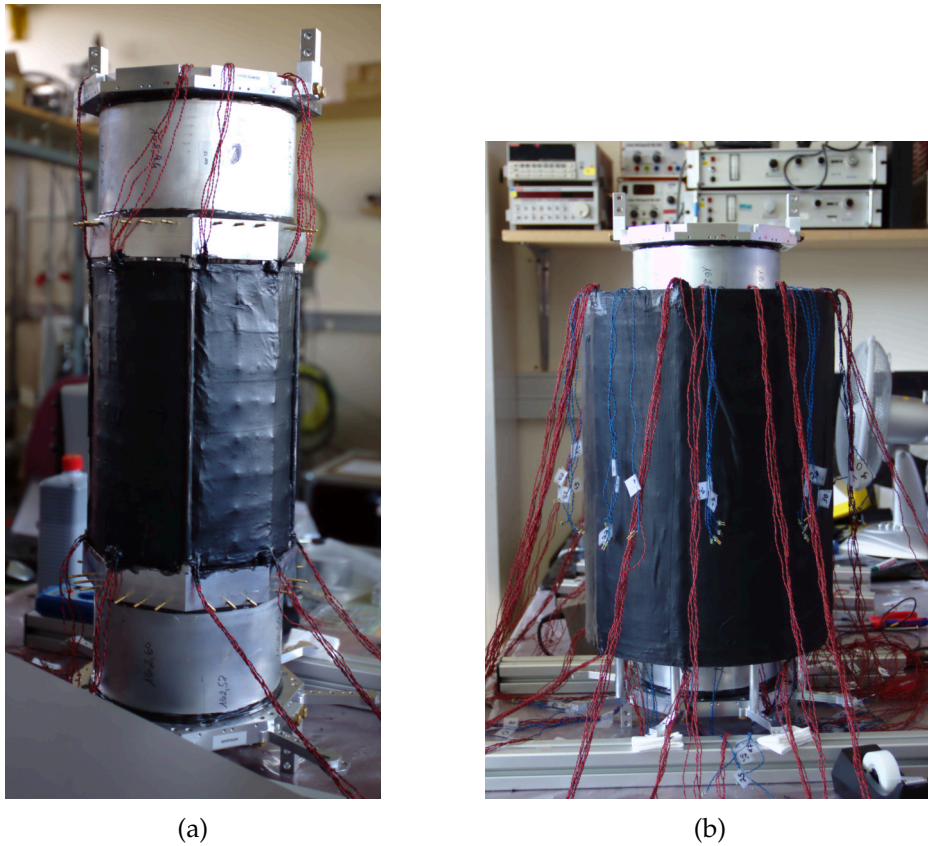


Figure 4.12.: Inner (a) and outer (b) layers covered with black tape and latex, making them light-tight.

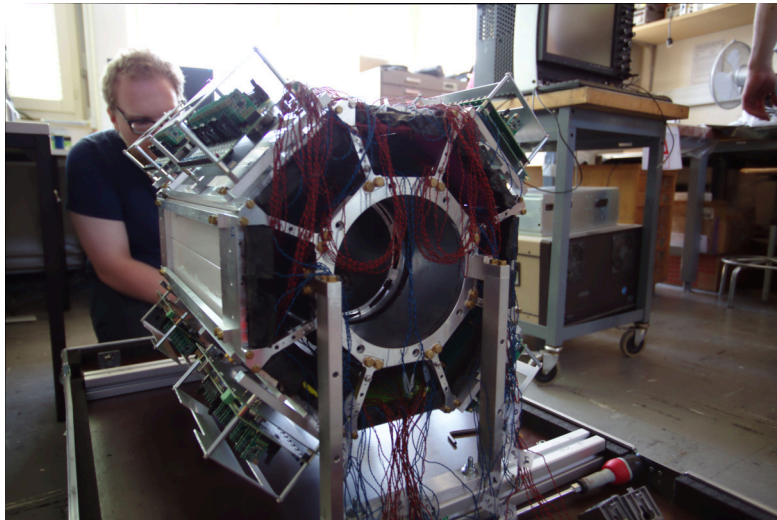
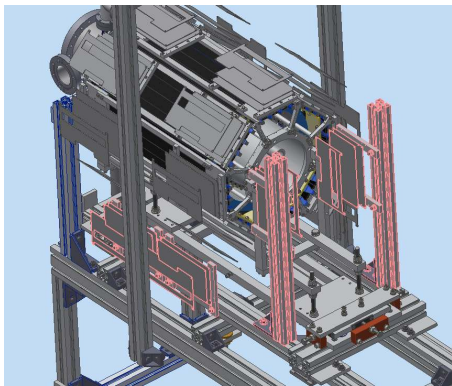
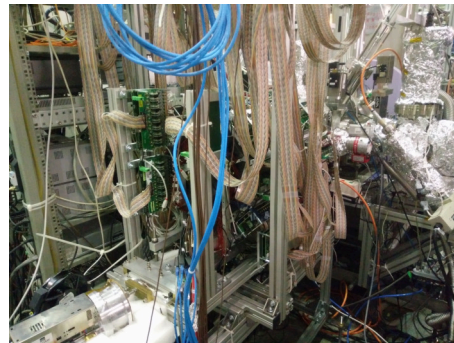


Figure 4.13.: The completed detector with fibre and bar layers installed. The red cables come from the fibre SiPMs, the blue cables from the bar SiPMs



(a)



(b)

Figure 4.14.: The distribution of the preamplifier boards on and around the detector. (a) is a render by D. Priztauz-Telsnigg, (b) is a picture of the final setup.

5. Data Acquisition

This chapter focuses on the changes made to the data acquisition system in order to accommodate the readout for the fibre detector component. As the fibre detector is mostly independent from the bar hodoscope, this chapter is split into two main sections. The first section gives a brief overview of the existing system as seen in [27], the second section describes in detail new and modified components. The slow control system for the detector shall also be included here.

5.1. Basic DAQ System

The DAQ depends heavily on VME (Versa Module Europa) and NIM (Nuclear Instrumentation Module) modular electronics, which are installed in a standard 19 inch rack on a platform above the ASACUSA experimental area. The NIM electronics are primarily used for the trigger logic (see also fig 5.1, and appendix C.5) and consist of the modules listed in table 5.1, the VME crate contains the main data acquisition hardware for all detector components, listed in table 5.2.

Table 5.1.: NIM modules used for triggering and signal transfer. The order reflects the order of the modules in the NIM crate from the left. The two modules after the break are located in a different crate, albeit in the same rack. These additional modules are mainly used for the recording of the mixing signal, this is discussed further in section 5.2.3

Manufacturer	Model	Function
CAEN	N93B	Dual timer
CAEN	2255	Dual timer
LeCroy	465	4-fold coincidence unit
LeCroy	4616	ECL/NIM/TTL translator
LeCroy	429A	Logic fan-in/fan-out
LeCroy	429	Logic fan-in/fan-out
SMI		Differential to single-ended converter
LeCroy	429A	Logic fan-in/fan-out
CAEN	N93B	Dual timer
LeCroy	4616	ECL/NIM/TTL translator

Table 5.2.: VME modules used in the DAQ system. Components added during this work are marked red. The ordering reflects the order of the modules in the VME crate from the left

Manufacturer	Model	Function
Struck	SIS3100	VME controller, link to DAQ PC
Struck	SIS3820	Scaler
CERN	TTCvi Mk2	Clock source
CAEN	V1495	FPGA programmed for trigger calculation
Clear Pulse	80057	BGO data recorder
CAEN	V1190B	Time-to-digital-converter for fibre detector (64 channel)
CAEN	V1190A	Time-to-digital-converter for fibre detector (128 channel)
CAEN	V1742	Waveform digitiser for bar hodoscope (5 modules)

The VME hardware is controlled by a DAQ server that is connected to the electronics via an optical cable. The PC contains a SIS1100 PCIe (Peripheral Component Interconnect express) card for this optical link and communication with the VME controller. Furthermore, the DAQ server is running CERN Scientific Linux 6 and contains a hardware RAID (Redundant Array of Independent Disks) system for data storage.

5.1.1. MIDAS

MIDAS (Maximum Integrated Data Acquisition System) is a modular DAQ software developed by the Paul-Scherrer-Institut (PSI) in Switzerland and the Tri Meson Facility (TRIUMF) in Canada [44]. It comprises of multiple mostly independent parts that share information over an online database (ODB), listed in table 5.3. These components can be distributed among multiple machines for larger experiments, however, for the antihydrogen detector a single machine is sufficient.

Table 5.3.: Main software components of MIDAS

Name	Function
mserver	Communication between components, ODB management
mlogger	Provide ring buffer handles, storage of measured data
mhttpd	Provide web interface for starting and stopping the DAQ
one or more frontends	DAQ electronics communication, reading data

The first three components in table 5.3 are provided by the default MIDAS installation and form the basic experiment infrastructure. The mserver is the most fundamental component, as it provides the communication in between the other components and

5. Data Acquisition

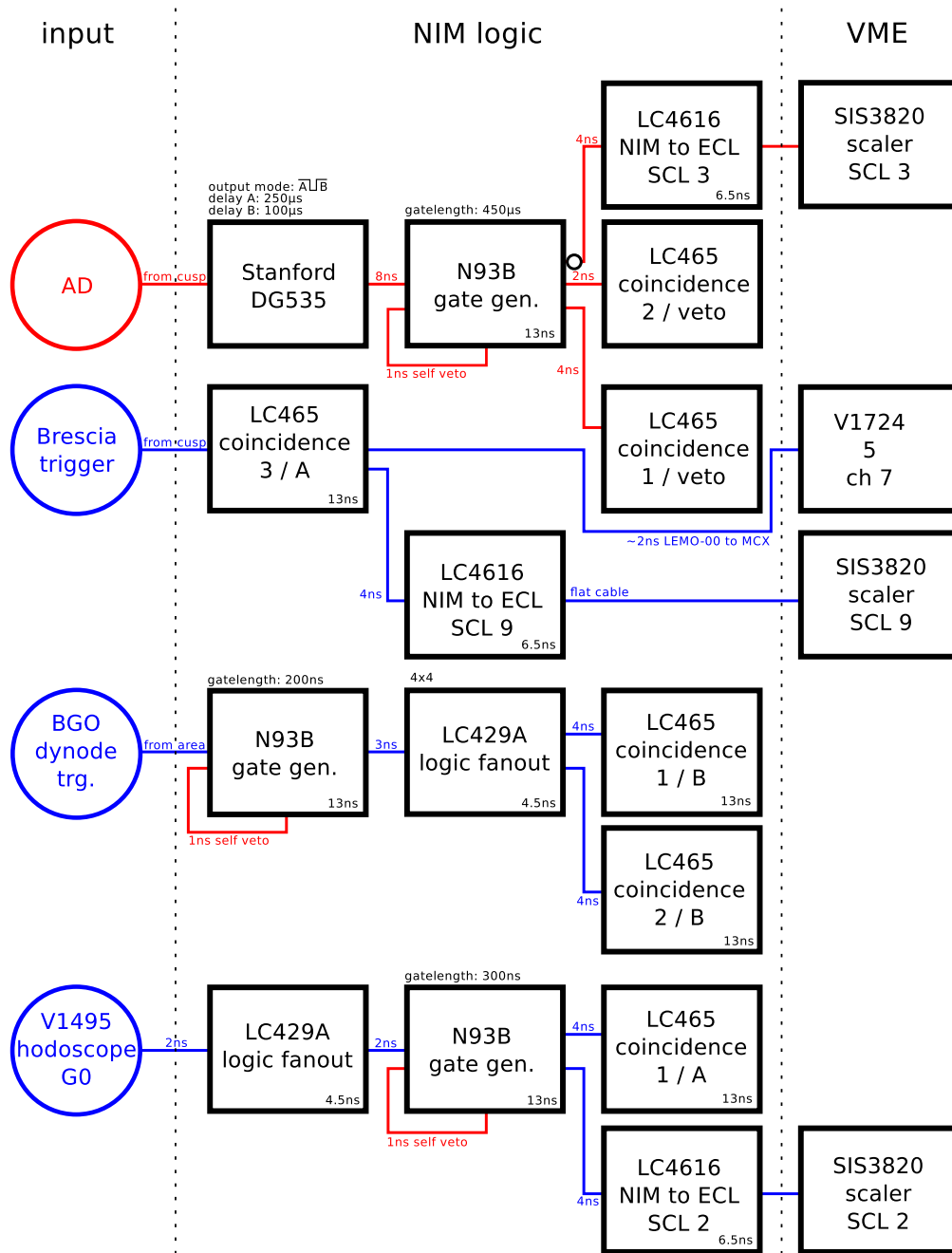


Figure 5.1.: Pathway of the trigger in the basic setup. Currently only the BGO dynode trigger and the FPGA (V1495) trigger are in use. The DAQ modules and the VME controller are connected to the coincidence unit via a fan-in/fan-out module. Vetos are drawn in red, the times given on the nodes indicate the delay added. For the exact pathway of the trigger after the coincidence unit, please refer to appendix C.5 or [27, 28]. Courtesy C. Sauerzopf.

acts as a supervisor for the online database. However, since in this experiment there is only one frontend, the `realEventFrontend`, it can run without the `mserver`, but this mode of operation bears a high risk for corruption of the ODB and problems with the data logging.

Data logging is done via the `mlogger`. The `mlogger` creates a ring buffer in the PC's random access memory (RAM) and provides the frontends with a handle to access this ring buffer. Per default, data is saved in a binary format whose specification is part of the MIDAS project, so-called MIDAS files. Output into other formats is possible, however, output into MIDAS files is usually the fastest while maintaining a manageable file size. It should also be mentioned that there is also a special logger for non-time-critical data, the so-called `lazylogger`. This feature is not in use for the setup described in this thesis at the moment, however, it could be used to record secondary data like temperatures or settings.

`mhttpd` is a self-contained web server that hosts a web-based graphical user interface (GUI) for the MIDAS system. It also provides an accessible way to interact directly with the ODB. This is especially helpful since there are some settings that are frequently changed during the development and setup phase. Storing and recalling them to and from the ODB avoids having to recompile the program for every miniscule change. The web server also provides an integrated electronic logbook. This logbook is fully integrated, however, it is functionally the same as the wide spread electronic logbook `elog`, also developed at PSI. The similar backend of the MIDAS logbook and the `elog` allows for a synchronisation of two instances of these softwares. In the case of the hodoscope, the MIDAS logbook is synchronised with a `elog` installation on the SMI's servers in Vienna.

All the components described above, `mserver`, `mlogger`, and `mhttpd`, require the user only to enter the correct settings and provide the correct environment. However, the final main component of a MIDAS installation, the frontends, requires more contribution by the user. MIDAS provides a framework and a set of predetermined functions for the creation of a experiment specific frontend written in C++. Given that a frontend is required to directly access the DAQ hardware, device drivers are needed. The MIDAS source package contains a collection of drivers that provide a basic hardware interface, so-called low-level drivers. These packaged drivers encompass some of the most used electronics, however, for the bar hodoscope new drivers for the waveform digitisers and the BGO readout system had to be developed [27]. The counterpart of the low-level drivers, the high-level drivers, provide more abstracted functions to interact with the hardware, but are usually implemented by the user since they are a part of the frontend.

The frontend used for the ASACUSA detector is called `realEventFrontend` and handles initialising, triggering, and data recording for all detector components. `realEventFrontend` is the only frontend used in the ASACUSA detector, and so has a quite high workload.

To mitigate this, some functions, specifically those which are polling a value, such as the run number, periodically, are executed in a separate thread.

The data readout happens event-based whenever a trigger interrupt is received at the front panel interrupts of the SIS3800 controller. When the interrupt is received, a veto is put in place to avoid further triggering before the readout cycle is completed. Next, the frontend requests a handle on the MIDAS ring buffer and proceeds to fill the buffer with data from the electronics.

The buffer is written to the output file by the mlogger. In the buffer as well as in the output file the data is organised by events. Every trigger creates a new event, and each event contains all data recorded at that point encoded in so-called data banks. Within the data banks the data is usually stored in the form of hexadecimal data words as they are read from the output buffers of each particular system, the conversion to usable values has to be done in the next step, the analyser.

5.1.2. Analyser

The analyser, or more accurately the pre-analyser since it prepares data for the actual analysis, reads the MIDAS files and converts the raw data into ROOT files, the default file format of the eponymous CERN data analysis package [45]. In order to do that, it uses libraries from both the MIDAS and ROOT projects. The MIDAS library *MidasFile.h* (a part of the ROOTANA package) provides functions to access the MIDAS output files, and *TROOT.h* from the ROOT sources provide methods to handle ROOT files.

Most of the data banks in a typical MIDAS file from the hodoscope DAQ can be simply decoded and saved. However, the analysis of the waveform digitiser data is more complex, so this task is mainly facilitated by the so-called *waveformlibrary*. This software library was written by C. Sauerzopf and is explained in detail in [27, 46]. The most important points are that it can be used to analyse arbitrary waveforms and that it incorporates a plugin-based system to facilitate this. In the case of the ASACUSA detector, it is used to calculate the collected charge as well as the leading edge and constant fraction time stamps for each recorded waveform. Furthermore it also uses a Fourier-transform-filter mechanism to reduce high-frequency noise on the waveforms.

These calculated data, along with the data from the BGO and some general variables are saved into one ROOT file per run. Within the ROOT files, data are organised into so-called trees. These trees can have multiple branches which in turn can subdivide into multiple leaves. For the detector data a rather simple structure was chosen, with four trees that only have leaves and no branches or sub-branches. The four trees are the *HBarEventTree* and the *ScalarDataTree*, and the secondary trees also created by the analyser, the *ManualEventTree* and the *ClockEventTree*. A description of the fields in the data trees can be found in appendix C.4.

5.1.3. SiPM Amplification and Slow Control

The SiPMs of the bar hodoscope are connected to amplifying frontend electronics. In the beam time years before 2016, these were the so called Intelligent Frontend Electronics for SiPMs (IFES), here, only a brief overview is given, as a thorough description including schematics can be found in [27, 28, 47]. In 2016, new electronics were introduced, and subsequently also used for the fibre detector. This shall be discussed in section 5.2.4.

The IFES boards support two input channels each and provide an amplified analogue signal and a digital time over threshold (ToT) signal. The whole amplification circuit is designed to use differential signal throughout and the output is a balanced differential signal. Differential signals have two advantages. First, they are much more resistant to electronic noise, which is of course very prevalent within the AD experimental zones. The noise is additive on both channels and so vanishes in a difference. The second advantage is that a differential connection is per definition ground-free, avoiding any issues that stem from different grounds or ground loops between the detector and the DAQ.

The time over threshold signals produced by the onboard discriminator adhere to the low voltage differential signal (LVDS) standard, which, along with ECL (emitter-coupled logic), is very commonly used in data recording and signalling electronics.

Parameters like the amplification gain and the threshold of the time over threshold can be set from remote via a slow control system, the amplification gain has also a coarse manual setting via a potentiometer on the board. The current value of the amplification can be read out via a jumper on the board, the threshold setting have to be measured, for instance with an oscilloscope. To facilitate the remote control, all IFES modules are connected by a SPI bus in a daisy chain configuration. The input of the first board and the output of the last board of the chain are connected to a specially made Arduino shield, fitted on an Arduino Leonardo. The operation principle of the daisy chain is that all commands are issued sequentially and each command received by a board issues a ready signal to the next board, which can then in turn accept the next command and so on. For remote communication with a computer, the Arduino Leonardo is connected to an Arduino Yun, which has network capabilities and a miniature Linux running on a microprocessor.

Once the settings are finalised, they can be saved to the Arduino's onboard electrically erasable programmable read-only memory EEPROM, so that they are available after a power cut. However, this should only be done in moderation since EEPROMs have a limited number of write cycles, especially compared to commonly known memory hardware such as magnetic hard drives.

5.2. Advancements in the DAQ System

In this section the differences to the basic DAQ system described before are the main focus. The primary change to the DAQ is the integration of the electronics and software used for the fibre detector. Also described are changes to the DAQ and slow control system as a whole, however these are mostly smaller differences.

5.2.1. Accessing the V1190 TDC Module

As mentioned before, the fibre detector's data is recorded by two CAEN V1190 TDC modules. One of the modules has 64 channels (V1190B) and one has 128 channels (V1190A), both have flat-band cable inputs on their front panels that accept LVDS and ECL signals. These are Robinson Nugent P50E-068-P1-SR1-TG high density connectors, each with 32 channels differential channels plus four not connected pins. With adaptor cables each port is split in two regular 17+17 pin header connectors, so in total there are 16 ports with pin head connectors available. This configuration with two different module types was chosen due to the fact that the 64 channel module was already available from a previous experiment, and that the two modules have completely identical VME interfaces and capabilities. Additional connectors on the front panel are the trigger input and the control register input. The trigger input is a double, bridged LEMO 00 connector. In the DAQ, the main trigger signal is connected to one input, the other one is terminated by a $50\ \Omega$ resistor. The trigger signal is the same as shown in figure 5.1, however there is a small addition in the form of a or-relation to the mixing start signal, further elaborated on in section 5.2.3 The control register input is a 8+8 pin header connector, however, since only the clock input is in use, the input is connected by a 2 pin plug. The clock signal comes from the CERN TTCvi clock source via an ECL/NIM/TTL translator as the control register only supports differential ECL signals.

For some early tests and driver development, a similar module was used, the V1290N, since the V1190 modules were not available at that point. This module has the same capabilities, but features LEMO 00 connectors instead of a flat-band cable and 16 channels. The VME interface for the V1290 is similar enough to the V1190 to function with the same driver, which makes the module a good replacement for testing. Figure 5.3 shows the setup used during development, comprising of one V1290N alongside a V1190A and other modules.

All the modules mentioned above use the HPTDC (high precision TDC) TDC chip developed by CERN [48]. In the configuration used in the V1190 modules, the chip allows up to 100 ps resolution, in the V1290 units, the high-precision mode that allows up to 25 ps is used. Since the measurement of the time over threshold, in the terminology of the manufacturer called pair or width measurement, can not be done in the high precision mode, the V1290 used for testing has to be set to a lower resolution.

5. Data Acquisition



Figure 5.2.: The DAQ setup used for early testing, from the left: SIS3100 controller, SIS3820 scalar, V1290N TDC, V1190A TDC. On the rightmost side a V1742 module is shown, however, this was excluded from the test software due to unresolved hardware errors.

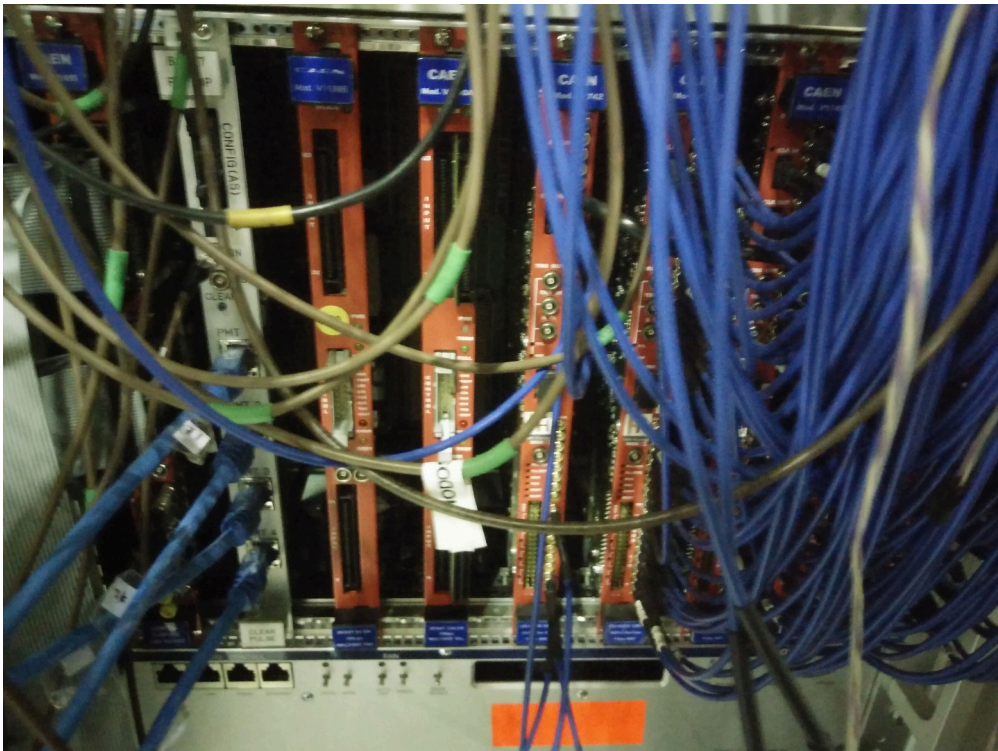


Figure 5.3.: The positioning of the TDC modules in the DAQ setup at CERN. The TDC data cables are not connected for a better view. Right of the TDCs, the V1742 digitiser are situated, located left of the TDCs are the CP80057 BGO data recorder and the V1495 FPGA.

The V1190 series offers two modes of data taking and several modes of data transfer [49]. Data recording can be done continuously or in the so-called trigger matching mode, the data transfer can be done in several data transfer modes that the VME standard comprises. In the trigger matching mode, the modules accept a trigger and forward it to the chips. In the chips, hits that were recorded during a predefined trigger window relative to the received trigger are bundled into an event and written into the output first-in-first-out buffer (FIFO). The pure HPTDC chips only record data that happened before the arrival of the trigger, however, the V1190 module also allows a so-called straddling trigger window, which means that the trigger can be within the trigger window. This is done by imposing an artificial delay on the trigger, so that the trigger window is always before the trigger time. An important point here is that for a successful measurement of the time over threshold, both the leading and trailing edge of the signal have to be recorded in the trigger window, for leading and trailing edge measurements alone it is sufficient if that edge is recorded.

For the ASACUSA detector the trigger matching mode was chosen, since its behaviour is similar to that of the waveform digitisers which also are triggered and produce output of what happened in a window before the trigger. Another advantage of the trigger matching mode is that since the hits are organised into events, the TDC data can be seamlessly integrated into the existing data structures. As data transfer mode, the VME D32 output buffer data transfer was chosen. Since each trigger received from the DAQ produces one event, which is then read out and cleared, this simple transfer mode is sufficient. However for other use cases, such as in high energy physics, the block transfer or continuous block transfer might offer an advantage. In the D32 output buffer transfer mode, data words are read from the output buffer until a global trailer to the event is met, after the data is read the output buffer is cleared. Normally, only one event is generated between readouts, however, to ensure that no data is cleared before readout and subsequently falsely cleared out, the amount of data words in the output buffer was counted at every step for different event rates during early development. In order to have more flexibility in the analysis, no identification and filtering of data words is done during readout. Once the system is fully functional and all parameters for the analysis are fixed, certain data words could be excluded from the readout, such as headers, trailers and debug messages. To still gain information about errors during the runtime, a special status register is read out and computed in the frontend to produce error messages if necessary.

The readout is handled by the the low- and high-level drivers and the readout function in the main part of the frontend. MIDAS includes a low-level driver for V1190B modules, which can also be used for V1190A and V1290 modules, since the low-level driver does not touch on any of the differences between the modules. However, the low-level driver had to be expanded by a few functions needed in the high-level driver, these are shown in the listing 5.1. The output of errors at runtime makes use of the `v1190_GetStatusRegister()` function, the `v1190_GetDummyValue()` and `v1190_WriteDummyValue()` functions are used for a periodic health check on the mod-

ules. If the modules were offline or there were problems with the data connection, the dummy value could either not be written or not read correctly. `v1190_GetFirmwareRevision()` was only used during development and early setup to determine if a firmware update for one of the two modules was necessary. Another function was added to the low-level driver, but not yet used. This function would take in multiple commands to write to the internal microprocessor of the module and write them sequentially using the same connection. That would speed up the initialisation of the system at the start of the frontend, but since the frontend is usually started and stopped before the experiment happens this was deemed unnecessary for the 2017 beam time. Headers for the functions mentioned above as well as the used VME addresses were added to the low-level driver header file.

The high-level driver was newly written during this thesis, however, to maintain compatibility and consistency among the components of the frontend the V1190 driver was modelled after the driver of the waveform digitiser. Drivers such as this provide high-level, meaning a high level of abstraction from the hardware, to other programs. The V1190 driver does this by providing a class containing all functions needed for the operation of the frontend. The most important functions are the `setup()` and `read()` functions, that get called at the startup and the readout, respectively.

`setup()` initialises the module by issuing a software reset signal and sets the parameters for the experiment by writing to special registers of the module's microcontroller. A listing of the section with the microcontroller commands can be found in appendix C.7, and the settings are summarised in table 5.4. Some of this settings have to be considered as volatile, these are the trigger window parameters and the resolution settings, as these may need to be set differently depending on the requirements of the experiment. The setup function also established a connection to the MIDAS ODB, as some settings, for instance the trigger window parameters, can be set via the ODB or the web interface provided by `mhttpd`. This was implemented due to those settings being changed often, especially in the development and integration period.

For an experiment with high precision, the trigger subtraction setting in table 5.4 turned out to be especially important. The trigger is recorded with the precision of the internal clock which runs at 40 MHz, so the possible time-steps are 25 ns wide. This means that if the trigger is subtracted from the values internally, the values could gain an offset of up to 25 ns. To avoid this, the trigger signal is also recorded on one of the regular inputs, so it that it can be used to do an external subtraction of the time stamps with a high precision in the analysis. A possible jitter in this case is additive to both signals and should therefore disappear in the difference.

The extra search margin and reject windows could provide an additional time before and after the trigger window. If hits fall into these additional time intervals, they are simply counted but their time structure is not recorded. For this setup however, both options are not in use. All terms related to the trigger are visualised in figure 5.5.

```
520 int v1190_GetFirmwareRevision(MVME_INTERFACE *mvme, DWORD base)
521 {
522     int cmode, rev;
523     mvme_get_dmode(mvme, &cmode);
524     mvme_set_dmode(mvme, MVME_DMODE_D16);
525     rev = mvme_read_value(mvme, base+V1190_FIRM_REV_R0);
526     mvme_set_dmode(mvme, cmode);
527     return rev;
528 }

530 int v1190_GetDummyValue(MVME_INTERFACE *mvme, DWORD base)
531 {
532     int cmode, dum;
533     mvme_get_dmode(mvme, &cmode);
534     mvme_set_dmode(mvme, MVME_DMODE_D16);
535     dum = mvme_read_value(mvme, base+V1190_DUMMY16_RW);
536     mvme_set_dmode(mvme, cmode);
537     return dum;
538 }

540 void v1190_WriteDummyValue(MVME_INTERFACE *mvme, DWORD base, int value)
541 {
542     int cmode;
543     mvme_get_dmode(mvme, &cmode);
544     mvme_set_dmode(mvme, MVME_DMODE_D16);
545     mvme_write_value(mvme, base+V1190_DUMMY16_RW, value);
546     mvme_set_dmode(mvme, cmode);
547 }

548 int v1190_GetStatusReg(MVME_INTERFACE *mvme, DWORD base)
549 {
550     int cmode, data;
551     mvme_get_dmode(mvme, &cmode);
552     mvme_set_dmode(mvme, MVME_DMODE_D16);
553     data = mvme_read_value(mvme, base+V1190_SR_R0);
554     mvme_set_dmode(mvme, cmode);
555     return (data);
556 }
```

Listing 5.1: Functions added to the existing MIDAS low-level driver for CAEN V1190B/A modules.

Table 5.4.: Settings for the V1190 modules, see also [49]

Setting	Value	Description
Trigger Matching Mode	On	Sets the trigger matching mode
Trigger Window Width	1200 ns	Width of the trigger window
Trigger Window Offset	-300 ns	Offset of the trigger window in respect to the trigger
Trigger Subtraction	Off	No internal subtraction of the trigger time
Extra Search margin	0 ns	No extra search margin
Reject margin	0 ns	No reject margin
Edge Detection	Pair Mode	Enables the ToT measurement
Resolution	Leading Edge 3.2 ns, Width 6.25 ns	If the pair flag is set, these have to be set together in one data word
TDC Header/Trailer	On	Enables header and trailer data words in the output
TDC Error Mark	On	Allows the insertion of error data words in the output
Enable All Channels	On	Enables all channels

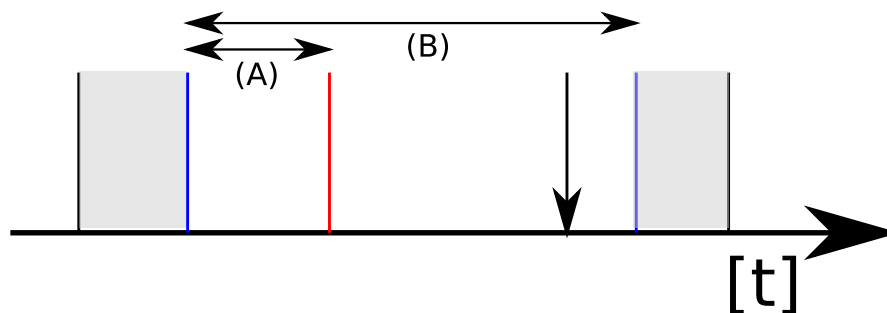


Figure 5.4.: The trigger window of the V1190 TDCs. The offset (usually negative) is added to the trigger (red line) to get the interval (A). The trigger window width is added to the lower end of (A) to get the full trigger interval (B). The shaded areas before and after the trigger window are the reject margin and the extended search margin respectively. The vertical arrow symbolises the recorded trigger which is delayed in respect to the trigger signal at the trigger input.

The `read()` function gets the data acquired by the TDC chips and hands it to the main frontend process, which writes it to the MIDAS data files via the `mlogger`. As described before, there is only one event per trigger and all provided data, including status messages is to be recorded. Due to this, the `read()` function can be written very compact. At first, the function checks if there are any data words to be read by polling the module's data ready flag (see listing 5.2). Should there be no data after $200\ \mu\text{s}$, the function times out and returns a negative state to the main program. If there is data ready to be read, the function proceeds to create a MIDAS bank in memory and gets the number of available data words in the output buffer. After another check that there are words to be read, the data are read event-wise, the data words written into the MIDAS bank, and the bank is closed. Afterwards the output buffer of the module is cleared and the function returns to the main program (see listing 5.3). During early development, functions to count the number of data words in the output buffer were included after every step to make sure all data are read. Additionally, at the start and the end of the `read()` function the status register of the module is read, and if there is an unusual status, an error message is produced.

In the frontend, objects of the `V1190` class get created for every connected TDC to handle the interaction between frontend and hardware. The MIDAS framework requires that frontends include a function that is run in certain intervals during a measurement run. This so-called frontend loop is used to check if all modules are still online. In the case of the `V1190` modules, this is done with the `v1190_WriteDummyValue()` and `v1190_GetDummyValue()` functions as explained before. The actual readout is invoked once a trigger is received on the front panels interrupts of the VME controller. At this point, all the `read()` functions of the detector components are called and the completed event is sent to the MIDAS ring buffer for saving (see listing 5.4).

5.2.2. Pre-analysing the Fibre Data

The pre-analyser's purpose is the translation of the MIDAS files in to a data format that can be used for analysis. In the analyser, functions for all detector components and other data such as timestamps are called in turn to create a ROOT file as output. The function that was added during the course of this thesis creates the ROOT leafs

```
118 for(int counter = 0; counter < 200; counter ++){
    if(checkEventStatus()) break;
    else{
120         nanosleep(&sleeptime, NULL);
    }
122 }
    if(!checkEventStatus()) return false;
```

Listing 5.2: The section of the `read()` function that polls for available data at the `V1190` module's output buffer.

```
132 bk_create(pevent, bname, TID_DWORD, &pdata);
    sleeptime.tv_sec = 0;
134 sleeptime.tv_nsec = 200000;
    nanosleep(&sleeptime, NULL);
136 int entries = getEventSize();
    if(entries>0){
138     v1190_EventRead(vme, vmeBaseAdress, data, &entries);
        for(unsigned int i=0; i<entries; i++){
140         *pdata++ = data[i];
        }
142 } else {
        return false;
144 }
146 bk_close(pevent, pdata);
```

Listing 5.3: The readout section of the function read().

```
482 // read waveform digitiser data
    for(int i=0; i<numOfV1742; i++){
484     digitisers[i]->read(pdata);
    }
486
    // BGO readout
488 bgoreadout->read(pdata); //for testing...
490
    //TDC readout
    for(int i=0; i<numOfV1190; i++){
492     tdcs[i]->read(pdata);
    }
494
    // assemble event
496 pevent->data_size = bk_size(pdata);
498
    // send event to ringbuffer
    rb_increment_wp(rbh, sizeof(EVENT_HEADER) + pevent->data_size);
```

Listing 5.4: The readout and data save section in the frontend.

marked red in the table C.8 (appendix C.4) and fills them with the data acquired by the frontend.

When called, the decode function searches for the banks associated with the TDC modules and steps through the data words contained within. The data words are 32 bit binary values that encode the data. To access it, the data words have to be decoded by binary masking and bit shift operations. The five right-most bits identify the word as either global header, TDC header, TDC trailer, global trailer, error mark or measurement word. Of course the most important ones are the measurement words, however there is also information to be gained from the other word types. Table 5.5 lists the position of the values that are most important for this work, a complete list can be found in [49].

Table 5.5.: Bits and the values they hold for different word types [49]

Word Type	Position of Data	Type of Data
All	[31...27]	Type of word
Global header	[26...5]	Event count
TDC header	[25...24]	Number of TDC chip
	[11...0]	Bunch ID, time stamp of trigger
Measurement	[25...19]	Channel number
	[18...12]	Time over threshold
	[11...0]	Leading edge time stamp
Error mark	[14...0]	Error flags

With the decoding, all values are also cast to C++ unsigned integers. The channel number that is found in the measurement words is the channel of the module, and corresponds to the inputs on the front. From this and the number of the module a continuous channel number that spans over all 192 channels can be calculated. The continuous channel number is in turn used to get the number of the corresponding fibre bundle in the detector via a lookup in a table. The lookup function divides the continuous channel number by 16 in an integer division, so that a number corresponding to a port on the TDC modules is found. With this number the right detector channel can easily be found in a table where the connected channels are organised in rows corresponding to the input cable ports, where each port also equals one of the amplifier boards. The number of the channel within each row is found by a simple subtraction of 16 times the port number from the continuous channel. An easily readable variant of this table is found in appendix C.6, table C.11.

During the decoding phase the function loops over each word in the bank, and if a measurement word is found, the contents get saved into a temporary vector. A C++11 vector container is used here since it is an efficient array of variable size, and there can be between zero and around a hundred measurement words in one event. In the vector, the channel, the leading edge time stamp, and the time over threshold are saved

sequentially.

After all words are decoded and the measurement data is written to the temporary vector, the function continues with writing to the arrays that represent the ROOT leafs.

There are leafs for both leading edge and time over threshold for both inner and outer layer of the fibre detector (tab. C.8 in appendix C.4). In the analyser, the inner and outer layer are distinguished by using negative and positive channel numbers respectively. A definitive distinguishing feature like this is needed since the channels on both layers start from 1, so there is an overlap in the range [1, 64]. This solution keeps the code relatively compact, however the channel number variable must be initialised as a signed integer.

Due to the fact that during tests multiple hits in one channel in one event were observed, the ROOT leafs are two dimensional arrays where each additional hit in one channel gets written into a new line, resulting in an array with as many columns as there are channels on that layer and as many filled rows as there are hits in the channel with the most hits in this event. Also integrated into the write-loop are checks for not properly initialised values. All used arrays get initialised with zero, however, sometimes very high or very low values can be observed despite this. These values are definitely errors, since they are always larger than what can be encoded in the number of bits used in the data words. However, this behaviour can be used to correct them with a simple if-clause checking for values higher or lower than the maximum or minimum possible.

In addition to the measurement data, there are also two special values that are saved in separate leafs. On one hand the triggers recorded via the regular inputs, and on the other hand the bunch ID, which is the trigger time stamp. The recorded triggers are delayed in respect to the trigger causing the readout due to the delay of cabling and electronics in between, however, it is more accurate since it is recorded with the same precision as the regular signals. The bunch ID can simply be read from the TDC header data words, the trigger timestamps have to be found within the measurement words. Since the channels at which the triggers arrive are fixed, this can be done by checking for this channel numbers.

5.2.3. Nanosecond Time Stamps

The topics of this section and the next one are smaller ones, however their scope is not only the fibre detector, but the whole DAQ. The internal 8.5 ns clock of the CAEN V1742 waveform digitisers can be read out and added to the data stream. However, this clock measures no absolute time, so whenever the clock's counter reaches its maximum, it rolls over to zero. In order to make the clock usable for absolute time measurement

during the experiment, two things are necessary: a reference point and an algorithm to calculate the time after the roll-over.

For the reference point a signal provided by the mixing trap can be used. This so-called mixing start signal indicates the beginning of the antihydrogen synthesis. In the setup as described in [27], the mixing start signal is only recorded by the scaler, however, to save the value of the digitiser clock along with the other data, the calculation has to be done at a point where the scalar data is not available in the program. To mitigate this the mixing signal is or-coupled with the actual trigger. The result is a trigger signal that is the same as the regular trigger plus one more trigger when the mixing signal is issued. This would create just an event filled with background, so to get a reliable time stamp, the mixing start signal is also fed into the spare waveform digitiser. By observing the channel of the mixing start signal on this module, a special mixing event can be created, and the regular time stamp of this event is used as a reference for the nanosecond time stamp.

The algorithm for the clock roll-over uses this signal to distinguish between events before the mixing, the event containing the mixing start signal, and events after the mixing. Before the mixing the function is inactive and only writes a placeholder into the data field. If the mixing event is recognised, some initial values for the calculation are determined and for events after the mixing the time stamp is calculated. In principal the calculation is based on two variables, `timeLoop` and `timeLoopBase`. `timeLoop` holds the time value since the last clock roll over, and `timeLoopBase` is the accumulated time of all clock cycles that have passed since the mixing start signal plus a correction for the clock cycle during which the mixing start happened. For this correction it is also necessary to know the time stamp of the start of the run, as MIDAS time stamps are expressed in UNIX time, that is seconds since 00:00, 1970/01/01. After the mixing start event, the calculation is straight forward: A comparison with the timestamp before shows if the clock rolled over since then, and if so `timeLoopBase` gets increased by one full cycle. Afterwards the current time stamp is calculated from the current value of the clock and the value stored in `timeLoopBase`. The code used for this can be found in listing 5.5, the value 9.126805504 on line 346 is the length of one full clock cycle in seconds, `clockReset` is the same value but expressed in nanoseconds.

5.2.4. New Amplifiers and Slow Control

In 2016 new amplifier electronics (fig. 5.6) were introduced to the bar hodoscope, and consequentially also used for the fibre detector. However, since these were not designed within the scope of the present thesis, they shall only be briefly described.

The new boards feature 16 instead of two channels and have an Arduino chipset integrated in a motherboard-daughterboard configuration. The additional channels are simply multiple versions of the IFES circuit next to each other on the daughterboard, the control and power supply daisy chain is realised in the printed circuit board (PCB).

5. Data Acquisition

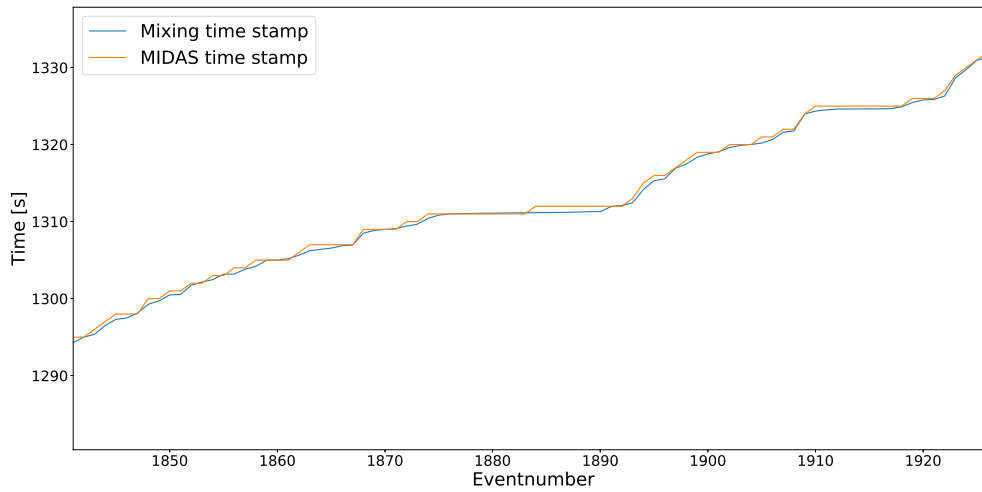


Figure 5.5.: A comparison of the MIDAS time stamp and the new nanosecond time stamp from a measurement run during a antiproton extraction. The x-axis is the event number, the y-axis is the time. The orange and blue lines are the MIDAS time and mixing time respectively. The mixing time follows the MIDAS time closely, but provides an almost continuous value instead of the single steps of the MIDAS time. This is especially obvious during times with a lot of events; the MIDAS time is flat, assigning each event the same time stamp, while the mixing time is different for each event.



Figure 5.6.: The successor to the IFES board. On the upper end, the SIPMs are connected, the small pin-header connectors provide analogue output, the large connector digital ToT signals. On the lower level motherboard, the power connector is seen on the left, and right to the middle the USB connector

```
340     if (data->isMixingSignal == true && whileMixing == false) {
342         whileMixing = true;
344         midastimedouble = (double) data->midasTimeStamp;
346         timeloop = data->SpareADCTimestamp[3]*8.5; //ns
348         adcOld = timeloop;
350         timetmp = (midastimedouble - runstartdouble)*1e9; //ns
352         timeloopBase = floor((midastimedouble-runstartdouble)
354 /9.126805504) * clockReset;
356         deltaT = timeloop + timeloopBase - timetmp;
358         timeloopBase -= deltaT;
360     }
362     if (whileMixing == true){
364         if ((data->SpareADCTimestamp[3]*8.5- adcOld) < 0){
366             timeloop = data->SpareADCTimestamp[3]*8.5;
368             timeloopBase += clockReset;
370         } else {
372             timeloop += (data->SpareADCTimestamp[3]*8.5- adcOld);
374         }
376         midastimedouble = (double) data->midasTimeStamp;
378         adcOld = timeloop;
380
382         data->mixingTimeStamp = (timeloop + timeloopBase)*1e-9;
384     } else {
386         data->mixingTimeStamp = -9999;
388     }
390 }
```

Listing 5.5: Main part of the calculation of the nanosecond time stamp. `clockReset` is a constant that has the value of one whole clock cycle

The power supply for the whole board is provided by a sturdy 2-pin connector taking in 5 V, which can be used with commercially available power supplies, as long as the plug is adapted. Onboard the power is fed into a circuit on the motherboard that provides both the stabilised reference voltage for the comparators and amplifiers, as well as the supply voltage for all the components. Due to the Arduino circuit, there is also a universal serial bus (USB) port, however, contrary to the Arduino specification, a USB type B connector is used, due to its improved mechanical stability. Also the power delivery pins of the USB port are not connected to reduce interference from the control hardware connected. To the onboard Arduino, the channels present themselves as eight daisy-chained IFES boards, so it can be controlled by the same serial commands as the old setup. However, a way to control all channels akin to the Arduino Yun in the old setup had to be found.

As part of the present work, a Python2-based control software was created to allow communication with all boards at once. In order to do this, the formerly identical firmware for all boards was swapped with an individual firmware for each board, that added a unique identifier (UID) along with a function that returns this UID. To easily distinguish between the boards serving the bar hodoscope and the fibre hodoscope, the UIDs are one digit for the bar hodoscope and two digits for the fibre hodoscope, as given in table 5.6.

Table 5.6.: UID ranges for the different hodoscope amplifier boards

UID Range	Associated Board Type
[0...7]	Bar hodoscope
[8...9]	Test boards
[10...20]	Bar hodoscope

Another addition to the firmware are arrays of which channels are connected to the board with that particular UID. These arrays are also position sensitive, meaning that the detector channel number is written at that index of the array that corresponds to the channel number of the board.

The control software expands upon a pre-existing class for communication with the IFES boards. While the old software was meant to be used with a system where all channels are connected to one Arduino, the new software has to accommodate for the fact that the channels are now subdivided into groups of 16. It is meant to be run on a PC that is connected to the boards via their USB cables. Also moving from a full-fledged PC to a more compact solution like a single-board computer, such as the BeagleBoard [50] or the Raspberry PI [51] is possible.

The boards are seen by the system as ACM (Abstract Control Model) devices and get assigned device nodes under Linux operating systems or COM ports under Microsoft Windows operating systems. Since this assignment is not constant (there are ways

to make it constant on one system, however, the software is meant to be seamlessly portable to other systems in case of a failure), the control software checks the assignment and creates a table connecting device nodes with board UIDs. This table is saved to speed up future executions, however it has to be refreshed after rebooting or changing connections. Another information gathered by the first startup and saved for later starts are the channels connected to each board.

With these two tables combined a lookup of the board UID and the device node of the board by inputting a hodoscope channel is possible. If the settings for one hodoscope channel have to be changed, i.e. during calibration, the channel and the new settings can be given to the program as input parameters and the program looks up the board where that channel is connected and sends the necessary commands to the right device node.

As a future update, this functionality can also be integrated into the MIDAS system. A prototype of this was created, however a fully functional implementation goes beyond the scope of this thesis. Also during the commissioning of the detector, it was discovered that the direction of the sockets on the boards and the sockets on the TDC modules are not the same, e. g. the two differential channels have the wrong sign. With the plugs on the cables flipped, the sign is correct, however there are now signal channels connected to the not connected pair that 32 + 2 IDC plugs have. To counteract this, the outermost lanes of the cables are cut and connected crosswise so that no signal is lost. In a future revision of the boards, the order of the connections between the amplifier electronics and the IDC sockets should be reconsidered to avoid this problem.

6. Summary and Outlook

6.1. Summary

In this thesis, an upgrade for the antihydrogen detector used by the ASACUSA collaboration was performed in order to improve background suppression and enable three dimensional tracking instead of the two dimensional methods used so far. The additional component makes use of scintillating fibres and silicon photomultipliers. The fibres are wound for one turn each along carbon tubes and held in place by plastic fastening rings. This ensures that the additional layers add as little high-Z-material to the detector as to not significantly increase scattering. Preliminary measurements taken with the used fibres and SiPMs before the construction work showed that the design choices made were feasible. Especially there is no significant crosstalk between the fibres, which ensures that a signal on an SiPM came from the associated fibre. However to achieve this, the fibres are clad in a thin layer of acrylic, so a small amount of active area is lost to that.

The SiPMs were prepared and soldered onto circuit boards, as well as cables for the readout. The fibres were cut, polished and bundled into groups of four, and every bundle was joined with one SiPM by the means of optical cement. For this glueing process, glueing guides were 3-d printed to ensure the correct positioning.

The finished bundles were wound into the support and locked in place with the fastening rings. On the top and the bottom of both tubes, end pieces were glued on. Afterwards they were light-tightened by applying multiple layers of black isolation tape and black latex paint.

For recording the data of the fibre layers, two CAEN V1190 TDCs are used. To integrate those into the DAQ system, drivers for the MIDAS DAQ framework have been written. The drivers were integrated with the existing frontend software.

A resolution of 7.72 mm lengthwise on the central axis of the detector is expected.

To make use of the raw data, the existing pre-analyser was modified and extended to be able to process data from the fibre detector. The processed data is written into ROOT files for easy access.

The detector was successfully used during the 2017 ASACUSA beam time at the AD, examples of the data taken by the fibre detector can be seen in figures 6.1 and 6.2. For a final analysis, a 3D tracking algorithm is under development by B. Kolbinger [17].

6. Summary and Outlook

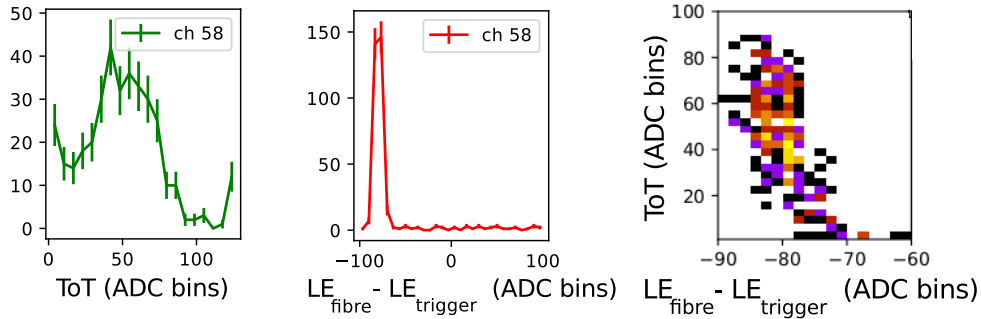


Figure 6.1.: Plots that exemplify the data recorded by the fibre detector. Shown are the time over threshold (left) the leading edge time of the signal with the trigger time subtracted (center) and a histogram time over threshold versus leading edge time (right) of one channel [17].

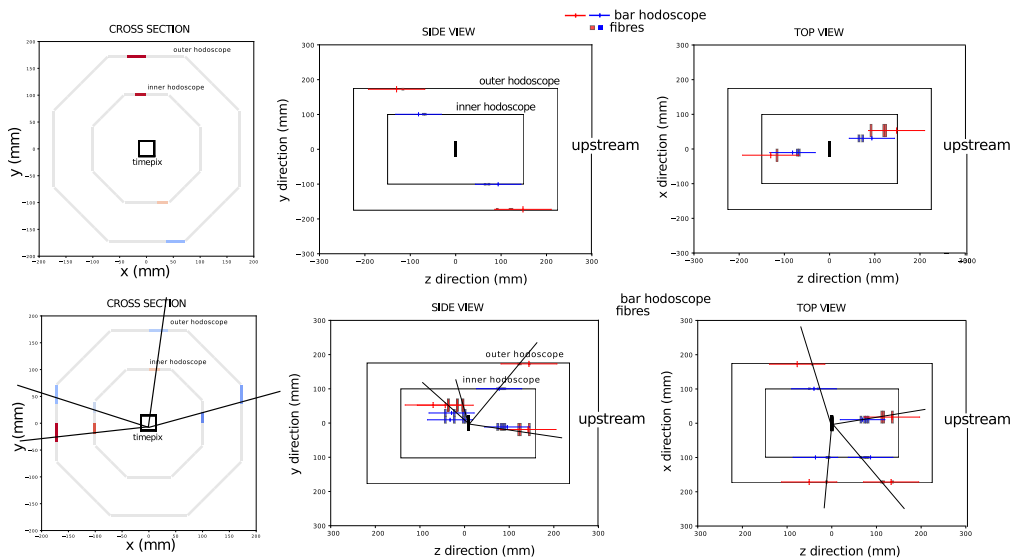


Figure 6.2.: Examples of reconstructed events. The top row shows a cosmic events and the bottom row a antiproton event. The red and blue lines indicate the coarse longitudinal information from the inner and outer bar hodoscope, the red and blue squares show the active fibres in the inner and outer layer. The reconstruction is still work in progress, so the black lines are not the final tracks but rather a visual aid drawn by hand. For this measurement, the central detector was replaced by the TimePix3 hybrid pixel detector, otherwise the detector setup was the same [17].

An additional timestamp with an accuracy of ~ 10 ns was introduced into the DAQ. This makes use of the internal clock of the CAEN V1742 waveform digitisers used for the bar hodoscope.

A new slow control system compatible with the also newly introduced pre-amplifier boards was created. This system runs on a single-board computer attached to the detector.

6.2. Outlook

The detector is working and preparing to take antiproton and antihydrogen data. Currently another ASACUSA experiment concerning annihilation studies is in preparation, and the hodoscope including the fibre detector would also be used for that. To ensure a stable operation, the frontend should be optimised in terms of the highest accepted event rate. At the moment, the highest event rate is around 50 Hz, however in the annihilation experiment, a much higher rate is possible in principle. This can be improved with an optimised readout, including the VME chained block transfer mode. In this mode all modules that support it can be read in a high speed serial manner over the same connection rather than opening and closing connections for each readout.

The problem of the few high-noise channels is still unsolved, however to investigate this further, the detector would have to be disassembled.

During the implementation of the new slow control it was found that the serial connection between the single board computer and some pre-amplifier boards is not functional, causing errors in the software. The affected boards should be checked and if necessary replaced in order to have the slow control working on all boards equally.

The slow control can also be integrated directly into MIDAS, as a so-called slow control frontend. This would have the advantage that everything detector-related can be controlled from the MIDAS web interface.

Appendix

Appendix A.

Used Acronyms

Table A.1.: Table of used acronyms throughout this thesis, capitalisation indicates letters that contribute to the acronym.

ACM		Abstract Control Model
AD		Antiproton Decelerator
AMT		ASACUSA Micromegas Detector
ASACUSA	Atomic Spectroscopy And Collisions Using Slow Antiprotons	
BGO		Bismuth-Germanium-Oxide
CERN	Conseil Européene pour la Recherche Nucléaire	
DAQ		Data AcQuisition
ECL		Emitter Coupled Logic
EEPROM	Electronically Erasable Programmable Read Only Memory	
FIFO		First-in/First-out
FIT		Field Ionising Trap
FI		Field Ioniser
GUI		Graphical User Interface

Appendix A. Used Acronyms

Table A.2.: Table of used acronyms throughout this thesis, capitalisation indicates letters that contribute to the acronym. (Cont. of tab. A.1)

HFS	High-Field Seeking/Seeker
HPTDC	High Precision Time to Digital Converter
IFES	Intelligent Frontend Electronics for SIPMs
LFS	Low-Field Seeking/Seeker
LHC	Large Hadron Collider
LVDS	Low Voltage Differential Signal
MAPMT	Multi Anode Photo Multiplier Tube
MIDAS	Maximum Integrated Data Acquisition System
Micromegas	MICRO MESH Gaseous Structure
MRE	Multi Ring Electrode
NIM	Nuclear Instrumentation Model
ODB	Online DataBase
PCB	Printed Circuit Board
PCIe	Peripheral Component Interconnect express
PIPS	Passivated Implanted Planar Silicon
PSI	Paul-Scherrer-Institut
PS	Proton Synchrotron
QFT	Quantum Field Theory
RAM	Random Access Memory
RFQD	Radio Frequency Quadrupole Decelerator
RF	Radio Frequency
SiPM	Silicon PhotoMultiplier
SME	Standard Model Extension
mSME	minimal Standard Model Extension
SPS	Super Proton Synchrotron
TRIUMF	TRI-University-Meson-Facility
ToT	Time Over Threshold
UHV	Ultra-High Vacuum
UID	Unique Identifier
USB	Universal Serial Bus
VME	Versa Module Europa

Appendix B.

Materials and Devices

Table B.1.: Table of used materials and devices. The NIM and VME electronics used can be found in chapter 5, tables 5.1 and 5.2. The constituents of the existing bar hodoscope can be found in [28].

Manufacturer	Device/Material
LeCroy	WaveRunner Zi 6
Peaktech	1070 digital multimeter
Fluke	87V True RMS multimeter
Saint Gobain	BCF-12 scintillating fibres, square, $2 \times 2 \text{ mm}^2$ (660 m)
Saint Gobain	BC-600 optical two component glue
KETEK	PM3350-EB SiPMs (163 pcs.)
Cikoni	Carbon tube $d = 167 \text{ mm}$
Cikoni	Carbon tube $d = 292 \text{ mm}$
Generic	Liquid black latex
Generic	Black isolation tape
D-Link	7 port USB 2.0 hub (2 pcs.)
Distrelec	USB cables (12 * 3 m)
Amphenol	34-wire twisted-pair flat-band cables (11 * 11 m)
Amphenol	IDC plugs, 34 pins (22 pcs.)
Distrelec	CAT6 S/FTP ethernet cable (20 m)
Beagleboard	BeagleBone black
SMI	Pre-amplifier boards (11 pcs.)
Generic	Various cables

Appendix C.

Additional Tables, Listings and Figures

C.1. Specifications of used Fibres and SiPM

Table C.1.: Specification of Saint Gobain BCF-12 scintillating fibres [42].

Quantity	Value
Core refractive index	1.60
Density	1.05
Cladding refractive index	1.49
Cladding thickness	4% of fibre size
Operating temperature	-20° C to +50° C
Radiation length	42 cm
Emission peak	435 nm
Decay time	3.2 ns
Photons/MeV	~ 8000

Table C.2.: Specification of KETEK PM3350-EB SiPMs. Values dependent on the overvoltage applied are given at the recommended overvoltage of 5 V [43].

Quantity	Value
Active area	$3 \times 3 \text{ mm}^2$
Micro-cell size	50 μm
Breakdown voltage	25 V
Photo Detection Efficiency at 430 nm	38 %
Dark count rate	500 $\frac{\text{kHz}}{\text{mm}^2}$
Signal rise time	< 1 ns
Recovery time	130 ns

C.2. Measurements during Design and Assembly

Table C.3.: Test measurements of the inner fibre layer taken during assembly of the fibre detector. The values are counts, the measurement time is 60 s.

Channel	With source	Without source	Channel	With source	Without source
1	480	44	33	560	25
2	1152	35	34	669	35
3	725	34	35	668	35
4	1032	48	36	633	23
5	657	59	37	471	25
6	1355	40	38	758	38
7	1149	39	39	690	34
8	1269	51	40	694	37
9	609	35	41	490	28
10	749	32	42	577	23
11	946	40	43	1014	36
12	766	21	44	1330	51
13	775	39	45	721	30
14	571	35	46	940	27
15	1354	41	47	768	32
16	973	38	48	589	31
17	885	45	49	800	31
18	749	41	50	503	30
19	517	37	51	1039	56
20	635	39	52	750	29

Table C.4.: Test measurements of the inner fibre layer taken during assembly of the fibre detector. The values are counts, the measurement time is 60 s. (Cont. of tab. C.3)

Channel	With source	Without source	Channel	With source	Without source
21	634	38	53	642	35
22	922	33	54	724	33
23	713	37	55	506	39
24	646	36	56	426	33
25	625	53	57	951	37
26	603	70	58	1041	40
27	426	39	59	869	50
28	623	37	60	1267	59
29	469	23	61	1093	33
30	548	74	62	1397	66
31	499	24	63	1692	43
32	449	25			

Table C.5.: Test measurements of the outer fibre layer taken during assembly of the fibre detector. The values are counts, the measurement time is 60 s.

Channel	With source	Without source	Channel	With source	Without source
1	3703	42	51	520	68
2	209	42	52	347	47
3	222	37	53	591	63
4	224	30	54	606	51
5	395	50	55	324	19
6	357	37	56	297	53
7	261	28	57	443	68
8	196	37	58	310	49
9	325	21	59	392	65
10	507	0	60	303	44
11	187	16	61	373	39
12	193	35	62	266	44
13	231	20	63	178	26
14	306	39	64	210	34
15	320	37	65	195	28
16	174	30	66	229	60
17	221	27	67	298	54
18	185	39	68	353	70
19	164	16	69	436	83
20	246	40	70	213	45
21	373	12	71	172	39
22	172	45	72	180	40
23	293	48	73	163	24
24	191	13	74	235	43
25	208	23	75	218	36
26	281	39	76	254	40
27	178	36	77	320	49
28	220	23	78	361	32
29	338	10	79	204	27
30	240	10	80	354	49
31	182	19	81	281	43
32	165	29	82	198	49
33	213	9	83	253	54
34	160	21	84	289	48
35	174	19	85	269	47

Table C.6.: Test measurements of the outer fibre layer taken during assembly of the fibre detector. The values are counts, the measurement time is 60 s (Cont. of tab. C.5).

Channel	With source	Without source	Channel	With source	Without source
36	269	29	86	250	40
37	212	30	87	301	43
38	210	40	88	441	53
39	214	45	89	357	59
40	249	35	90	439	63
41	180	21	91	206	29
42	238	21	92	499	68
43	188	32	93	346	42
44	213	28	94	164	29
45	275	40	95	316	57
46	326	13	96	260	34
47	426	33	97	219	53
48	279	42	98	176	30
49	467	79	99	380	64
50	459	51	100	237	38

C.3. MIDAS Data banks

Table C.7.: Data banks in the MIDAS files. Differences to the similar table seen in [27] are marked red.

MIDAS bank	System	Description
AxDA	Bar hodoscope	V1742 data, x=ADC number
AxTP		DRS4 temperature data, x=ADC number
TDCx	Fibre detector	V1190 data, x=TDC number
CPxD	BGO detector	BGO ADC data, x=PMT port
CPxR		CP80057 raw data, x=PMT port
CPxH		CP80057 event header, x=PMT port
CPQD		CP80057 time stamps
CPTD		CP80057 integrated charge
SCL0		Scaler
SCLT	Scaler timestamp	
MILT	Frontend software	
RUNN		Run number

C.4. Structure of the ROOT Trees

Table C.8.: Leafs in the hbarEventTree and manualEventTree ROOT data tree. The clockEventTree and BGOMIPEventTree contain only the BGO related entries and timestamps. Differences to the similar table seen in [27] are marked red. (continued on next page)

Leaf	Datatype
midasTimeStamp	int
midasMilliTimeStamp	double
mixingTimeStamp	double
isMixingSignal	bool
isADPulse	bool
LEtimeStampsInnerLayerUpstream	double[32]
LEtimeStampsInnerLayerDownstream	double[32]
LEtimeStampsOuterLayerUpstream	double[32]
LEtimeStampsOuterLayerDownstream	double[32]
LEtimeStampsSpare	double[32]
LEToTInnerLayerUpstream	double[32]
LEToTInnerLayerDownstream	double[32]
LEToTOuterLayerUpstream	double[32]
LEToTOuterLayerDownstream	double[32]
LEToTSpare	double[32]
CftimeStampsInnerLayerUpstream	double[32]
CftimeStampsInnerLayerDownstream	double[32]
CftimeStampsOuterLayerUpstream	double[32]
CftimeStampsOuterLayerDownstream	double[32]
CftimeStampsSpare	double[32]

Table C.9.: Leafs in the hbarEventTree and manualEventTree ROOT data tree. The clockEventTree and BGOMIPEventTree contain only the BGO related entries and timestamps. Differences to the similar table seen in [27] are marked red. (continued from last page)

Leaf	Datatype
ChargeInnerLayerUpstream	double[32]
ChargeInnerLayerDownstream	double[32]
ChargeOuterLayerUpstream	double[32]
ChargeOuterLayerDownstream	double[32]
ChargeSpare	double[32]
AmplitudeInnerLayerUpstream	double[32]
AmplitudeInnerLayerDownstream	double[32]
AmplitudeOuterLayerUpstream	double[32]
AmplitudeOuterLayerDownstream	double[32]
AmplitudeSpare	double[32]
InnerLayerUpstreamDRS4Temp	double[4]
InnerLayerDownstreamDRS4Temp	double[4]
OuterLayerUpstreamDRS4Temp	double[4]
OuterLayerDownstreamDRS4Temp	double[4]
SpareDRS4Temp	double[4]
InnerLayerUpstreamADCtimestamp	double[4]
InnerLayerDownstreamADCtimestamp	double[4]
OuterLayerUpstreamADCtimestamp	double[4]
OuterLayerDownstreamADCtimestamp	double[4]
SpareADCtimestamp	double[4]
TdcLEInner	int[128][64]
TdcLEOuter	int[128][128]
TdcWidthInner	int[128][64]
TdcWidthOuter	int[128][128]
TdcTriggerTime	int[2][2]
CUSPRunNumber	int
BGODataPortA	double[64]
BGODataPortB	double[64]
BGODataPortC	double[64]
BGODataPortD	double[64]
BGOTotalChargePre	double[4]
BGOHeaderPortA	int[2]
BGOHeaderPortB	int[2]
BGOHeaderPortC	int[2]
BGOHeaderPortD	int[2]
BGOTimeStamps	int[2]
BGORawDataPortA	int[32]
BGORawDataPortB	int[32]
BGORawDataPortC	int[32]
BGORawDataPortD	int[32]

Table C.10.: Leafs in the scalarDataTree.

Leaf	Datatype
midasTimeStamp	int
Timestamp	double
CUSPRunNumber	int
ScalarData	double[32]

C.5. Trigger flow diagrams

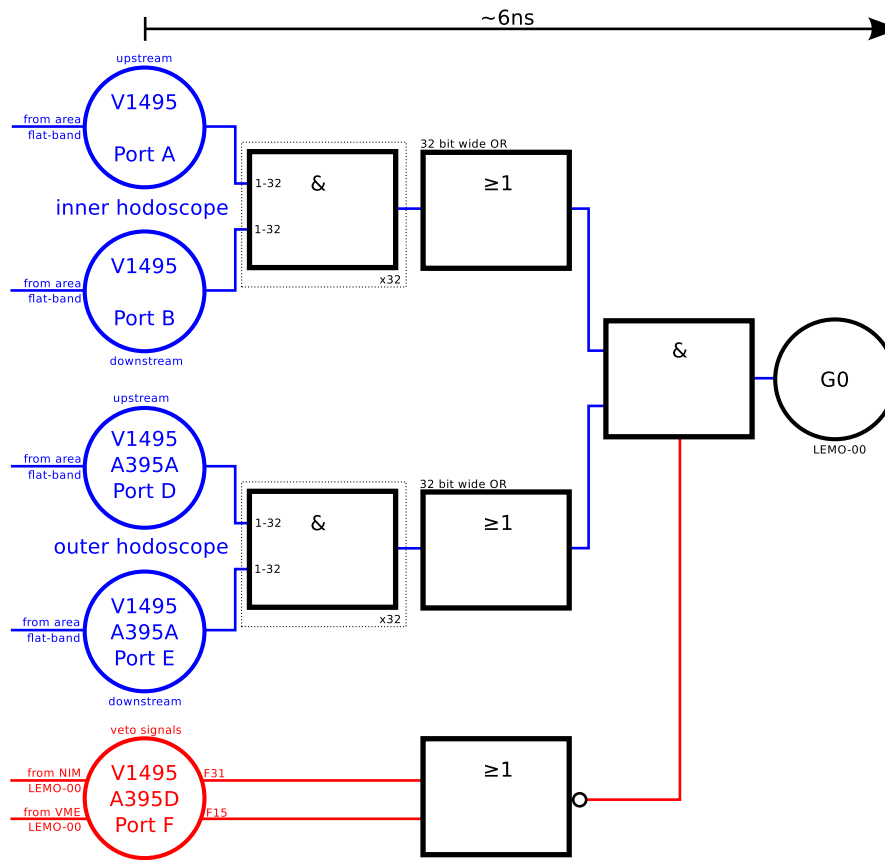


Figure C.1.: The trigger logic of the FPGA. Vetos are shown in red, the times given on the nodes are the delays added. Courtesy C. Sauerzopf [27].

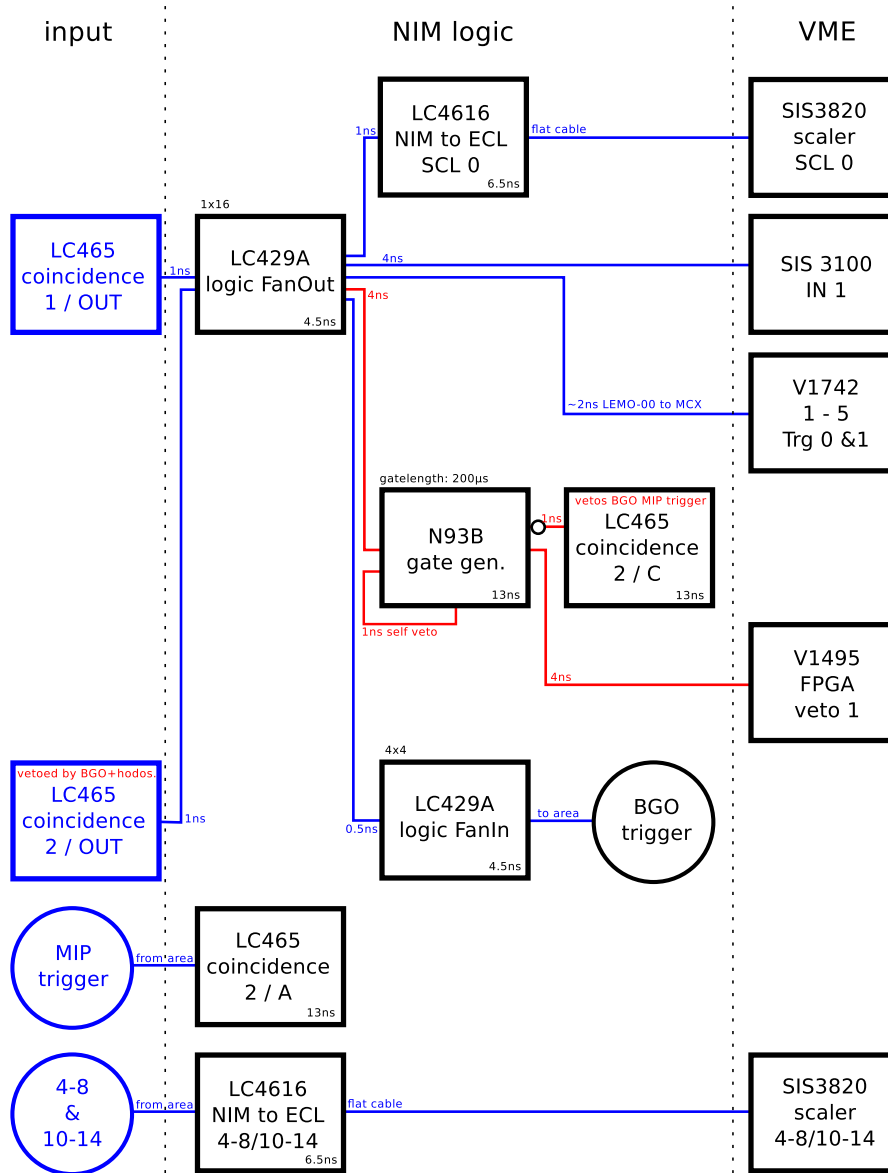


Figure C.2.: The trigger pathway after the coincidence unit. Vetos are shown in red, the times given on the nodes are the delays added. Courtesy C. Sauerzopf [27].

C.6. Fibre Detector Channel Mapping

Table C.11.: Mapping table between amplifier board channels and fibre detector channels. The amplifier boards are identified by their ID. Not connected channels are denoted by ‘–’, channels on the inner layer have the addition ‘*i*’, channels on the outer layer ‘*o*’.

Board ID	Board Channels															
	0	1	2	3	4	5	6	7	8	9	10	11	12	13	14	15
10	–	99 _o	91 _o	83 _o	75 _o	67 _o	59 _o	51 _o	–	–	–	–	61 _i	53 _i	45 _i	37 _i
11	50 _o	97 _o	89 _o	81 _o	73 _o	65 _o	57 _o	49 _o	60 _i	52 _i	44 _i	36 _i	59 _i	51 _i	43 _i	35 _i
12	8 _i	16 _i	24 _i	32 _i	1 _i	9 _i	17 _i	25 _i	22 _o	30 _o	46 _o	7 _o	15 _o	23 _o	31 _o	39 _o
13	–	98 _o	90 _o	82 _o	74 _o	–	66 _o	58 _o	–	–	–	–	58 _i	50 _i	42 _i	34 _i
14	63 _o	55 _o	96 _o	88 _o	80 _o	72 _o	64 _o	56 _o	–	57 _i	49 _i	41 _i	33 _i	56 _i	48 _i	40 _i
15	38 _o	47 _o	8 _o	16 _o	24 _o	32 _o	40 _o	48 _o	1 _o	9 _o	17 _o	25 _o	33 _o	41 _o	2 _o	10 _o
16	2 _i	10 _i	18 _i	26 _i	3 _i	11 _i	19 _i	27 _i	18 _o	26 _o	34 _o	42 _o	3 _o	11 _o	27 _o	19 _o
17	44 _o	36 _o	28 _o	20 _o	12 _o	4 _o	43 _o	35 _o	28 _i	20 _i	12 _i	4 _i	29 _i	21 _i	13 _i	5 _i
18	–	100 _o	92 _o	84 _o	76 _o	68 _o	60 _o	52 _o	62 _i	54 _i	46 _i	38 _i	63 _i	55 _i	39 _i	47 _i
19	53 _o	54 _o	61 _o	62 _o	69 _o	70 _o	71 _o	77 _o	78 _o	79 _o	85 _o	86 _o	87 _o	93 _o	94 _o	95 _o
20	6 _i	14 _i	22 _i	30 _i	7 _i	15 _i	23 _i	31 _i	5 _o	13 _o	21 _o	29 _o	37 _o	45 _o	6 _o	14 _o

C.7. Microcontroller commands in *v1190.c*.

```
26 code = 0x0000; // Trigger matching Flag
   if ((status = v1190_MicroWrite(vme, vmeBaseAdress, code)) < 0) retVal =
       false;
28
   code = 0x1500; // Disable subtraction flag
30 value = v1190_MicroWrite(vme, vmeBaseAdress, code);
32 //Extra search and reject margin = 0
   code = 0x1200; // Extra search margin
34 value = v1190_MicroWrite(vme, vmeBaseAdress, code);
   value = v1190_MicroWrite(vme, vmeBaseAdress, 0x0);
36
   code = 0x1300; // reject margin
38 value = v1190_MicroWrite(vme, vmeBaseAdress, code);
   value = v1190_MicroWrite(vme, vmeBaseAdress, 0x0);
40
   code = 0x2200; // Edge Detection
42 value = v1190_MicroWrite(vme, vmeBaseAdress, code);
   value = v1190_MicroWrite(vme, vmeBaseAdress, 0x0); // 0-> pair mode
44
   code = 0x2500; //Resolution setting LE 3.12ns, ToT 6.25 ns
46 value = v1190_MicroWrite(vme, vmeBaseAdress, code);
   value = v1190_MicroWrite(vme, vmeBaseAdress, 0x0605);
48
   code = 0x3000; // TDC Header/Trailer enable
50 value = v1190_MicroWrite(vme, vmeBaseAdress, code);
   value = v1190_MicroWrite(vme, vmeBaseAdress, 0x1);
52
   code = 0x3500; // TDC Error mark enable
54 value = v1190_MicroWrite(vme, vmeBaseAdress, code);
   value = v1190_MicroWrite(vme, vmeBaseAdress, 0x1);
56
   code = 0x4200; // enable all channels
58 value = v1190_MicroWrite(vme, vmeBaseAdress, code);
   value = v1190_MicroWrite(vme, vmeBaseAdress, 0x1);
```

Listing C.1: Microcontroller commands in the `setup()` function. Trigger window offset and width are omitted since they are overwritten by the ODB.

Appendix D.

Listings

5.1. Functions added to the existing MIDAS low-level driver for CAEN V1190B/A modules.	51
5.2. The section of the read() function that polls for available data at the V1190 module's output buffer.	53
5.3. The readout section of the function read().	54
5.4. The readout and data save section in the frontend.	54
5.5. Main part of the calculation of the nanosecond time stamp. clockReset is a constant that has the value of one whole clock cycle	59
C.1. Microcontroller commands in the setup() function. Trigger window offset and width are omitted since they are overwritten by the ODB. . .	83

Appendix E.

List of Figures

2.1.	A schematic drawing of the energy levels in (anti)hydrogen due to the hyperfine splitting.	7
2.2.	A Breit-Rabi diagram for the ground state hyperfine splitting of antihydrogen. On the right side the classification into HFS and LFS is shown [22].	8
3.1.	The CERN accelerator complex [31].	14
3.2.	The deceleration cycle of the Antiproton Decelerator [32]. In 2016 and 2017, the cycle is around 108 s long, due to a pause in between ejection and injection from and into the AD ring. However the length of this pause varies sometimes.	14
3.3.	An artistic representation of the double cusp field in the CUSP trap. Yellow are the magnetic field lines, red is the interaction zone, and blue is the beam of antihydrogen. Render by D. Pristauz-Telsnigg.	15
3.4.	From the top: Drawing of the CUSP MRE, electric trap potential and magnetic field. The trap potential shown is used in the direct injection mixing scheme [37].	17
3.5.	A schematic drawing of the beam line. Orange are HFS antihydrogen atoms, green LFS antihydrogen atoms [38]	19
3.6.	A rendering of the full beam line with all components marked. Render by N. Kuroda.	19
3.7.	The hodoscope with dimensions marked. The green arrow symbolises a beam of antihydrogen during an experiment.	21
3.8.	Examples for events that cannot be completely distinguished with two-dimensional analysis. Black is the impinging antihydrogen, green are pions from the annihilation and red are cosmic particles. The left hand side is the situation as seen in beam direction, the right hand side shows a perpendicular view.	23
4.1.	A drawing of the geometric model used for resolution estimation. . . .	26
4.2.	Drawings of the overlapping section of fibre bundles. Drawings by D. Pristauz-Telsnigg.	27

4.3.	A rendering of the detector including fibres and bars. The black arrows mark the outer diameter of the carbon tubes, the red arrow marks one of the 3D printed end pieces of the outer layer, and the green arrows mark the section where the old support is replaced by the carbon tube of the inner fibre layer. Render by D. Priztauz-Telsnigg.	27
4.4.	Pictures of the carbon tubes that make up the support for the fibre bundles.	29
4.5.	Detail shot of one of the plastic rings used to secure the fibre bundles in place. The black parts are the plastic bolts used to mount the rings to each other.	29
4.6.	The 3D printed prototype of the inner fibre layer used for measurements.	30
4.7.	Histograms of counts under threshold for different end treatments and two different threshold levels with a ^{90}Sr source. The histogram peaks are connected to provide a better visibility. Since the amplification electronics used output a negative signal, the values on the x-axis are negative and the measurement looks at events under the threshold.	31
4.8.	Setup for the crosstalk measurements. A 3D printed model of the outer layer is used. The Sr_{90} source is shielded by an aluminium block.	33
4.9.	Photos of the guide for glueing the fibres.	34
4.10.	Detail photo of a fibre in place. The securing ring and the overlap section can be seen. The protruding section of the SiPM board is always pointing inward, to avoid damages.	34
4.11.	The completely wound inner (a) and outer (b) layers.	36
4.12.	Inner (a) and outer (b) layers covered with black tape and latex, making them light-tight.	37
4.13.	The completed detector with fibre and bar layers installed. The red cables come from the fibre SiPMs, the blue cables from the bar SiPMs	37
4.14.	The distribution of the preamplifier boards on and around the detector. (a) is a render by D. Priztauz-Telsnigg, (b) is a picture of the final setup.	38
5.1.	Pathway of the trigger in the basic setup. Currently only the BGO dynode trigger and the FPGA (V1495) trigger are in use. The DAQ modules and the VME controller are connected to the coincidence unit via a fan-in/fan-out module. Vetos are drawn in red, the times given on the nodes indicate the delay added. For the exact pathway of the trigger after the coincidence unit, please refer to appendix C.5 or [27, 28]. Curtesy C. Sauerzopf.	42
5.2.	The DAQ setup used for early testing, from the left: SIS3100 controller, SIS3820 scalar, V1290N TDC, V1190A TDC. On the rightmost side a V1742 module is shown, however, this was excluded from the test software due to unresolved hardware errors.	47

5.3.	The positioning of the TDC modules in the DAQ setup at CERN. The TDC data cables are not connected for a better view. Right of the TDCs, the V1742 digitiser are situated, located left of the TDCs are the CP80057 BGO data recorder and the V1495 FPGA.	48
5.4.	The trigger window of the V1190 TDCs. The offset (usually negative) is added to the trigger (red line) to get the interval (A). The trigger window width is added to the lower end of (A) to get the full trigger interval (B). The shaded areas before and after the trigger window are the reject margin and the extended search margin respectively. The vertical arrow symbolises the recorded trigger which is delayed in respect to the trigger signal at the trigger input.	52
5.5.	A comparison of the MIDAS time stamp and the new nanosecond time stamp from a measurement run during a antiproton extraction. The x-axis is the event number, the y-axis is the time. The orange and blue lines are the MIDAS time and mixing time respectively. The mixing time follows the MIDAS time closely, but provides an almost continuous value instead of the single steps of the MIDAS time. This is especially obvious during times with a lot of events; the MIDAS time is flat, assigning each event the same time stamp, while the mixing time is different for each event.	58
5.6.	The successor to the IFES board. On the upper end, the SIPMs are connected, the small pin-header connectors provide analogue output, the large connector digital ToT signals. On the lower level motherboard, the power connector is seen on the left, and right to the middle the USB connector	58
6.1.	Plots that exemplify the data recorded by the fibre detector. Shown are the time over threshold (left) the leading edge time of the signal with the trigger time subtracted (center) and a histogram time over threshold versus leading edge time (right) of one channel [17].	64
6.2.	Examples of reconstructed events. The top row shows a cosmic events and the bottom row a antiproton event. The red and blue lines indicate the coarse longitudinal information from the inner and outer bar hodoscope, the red and blue squares show the active fibres in the inner and outer layer. The reconstruction is still work in progress, so the black lines are not the final tracks but rather a visual aid drawn by hand. For this measurement, the central detector was replaced by the TimePix3 hybrid pixel detector, otherwise the detector setup was the same [17].	64
C.1.	The trigger logic of the FPGA. Vetos are shown in red, the times given on the nodes are the delays added. Curtesy C. Sauerzopf [27].	80
C.2.	The trigger pathway after the coincidence unit. Vetos are shown in red, the times given on the nodes are the delays added. Curtesy C. Sauerzopf [27].	81

Appendix F.

List of Tables

2.1.	Branching ratios for $p + \bar{p}$ reactions. Only the highest fractions are shown. Branches without charged particles are omitted since they cannot be observed with the detector setup described in this thesis. From [24]. . .	9
4.1.	Dimensions of the carbon tubes supporting the scintillating fibres . . .	25
4.2.	Bias settings for the comparison between different end treatments . . .	28
4.3.	Test measurement with a bundle of fibres in a model of the inner layer. Measurement time is 300 s, the bias current is 1.48 μA	30
4.4.	Measurement of the crosstalk between two bundles. Measurement time is 300 s, the bias current is 1.33 μA for the bottom bundle and 4.77 μA for the top bundle.	32
4.5.	Length of the cut fibres. Top and bottom refer to the order of the fibres in on bundle, whereas bottom is the one that is further inside when installed.	32
5.1.	NIM modules used for triggering and signal transfer. The order reflects the order of the modules in the NIM crate from the left. The two modules after the break are located in a different crate, albeit in the same rack. These additional modules are mainly used for the recording of the mixing signal, this is discussed further in section 5.2.3	40
5.2.	VME modules used in the DAQ system. Components added during this work are marked red. The ordering reflects the order of the modules in the VME crate from the left	41
5.3.	Main software components of MIDAS	41
5.4.	Settings for the V1190 modules, see also [49]	52
5.5.	Bits and the values they hold for different word types [49]	55
5.6.	UID ranges for the different hodoscope amplifier boards	60
A.1.	Table of used acronyms throughout this thesis, capitalisation indicates letters that contribute to the acronym.	68
A.2.	Table of used acronyms throughout this thesis, capitalisation indicates letters that contribute to the acronym. (Cont. of tab. A.1)	69

B.1. Table of used materials and devices. The NIM and VME electronics used can be found in chapter 5, tables 5.1 and 5.2. The constituents of the existing bar hodoscope can be found in [28].	70
C.1. Specification of Saint Gobain BCF-12 scintillating fibres [42].	71
C.2. Specification of KETEK PM3350-EB SiPMs. Values dependent on the overvoltage applied are given at the recommended overvoltage of 5 V [43].	71
C.3. Test measurements of the inner fibre layer taken during assembly of the fibre detector. The values are counts, the measurement time is 60 s. . . .	72
C.4. Test measurements of the inner fibre layer taken during assembly of the fibre detector. The values are counts, the measurement time is 60 s. (Cont. of tab. C.3)	73
C.5. Test measurements of the outer fibre layer taken during assembly of the fibre detector. The values are counts, the measurement time is 60 s. . . .	74
C.6. Test measurements of the outer fibre layer taken during assembly of the fibre detector. The values are counts, the measurement time is 60 s (Cont. of tab. C.5).	75
C.7. Data banks in the MIDAS files. Differences to the similar table seen in [27] are marked red.	76
C.8. Leafs in the hbarEventTree and manualEventTree ROOT data tree. The clockEventTree and BGOMIPEventTree contain only the BGO related entries and timestamps. Differences to the similar table seen in [27] are marked red. (continued on next page)	77
C.9. Leafs in the hbarEventTree and manualEventTree ROOT data tree. The clockEventTree and BGOMIPEventTree contain only the BGO related entries and timestamps. Differences to the similar table seen in [27] are marked red. (continued from last page)	78
C.10. Leafs in the scalarDataTree.	79
C.11. Mapping table between amplifier board channels and fibre detector channels. The amplifier boards are identified by their ID. Not connected channels are denoted by '–', channels on the inner layer have the addition 'i', channels on the outer layer 'o'.	82

Appendix G.

Bibliography

1. Griffiths, D. *Introduction to Elementary Particles* ISBN: 9783527618477. <<https://books.google.ch/books?id=Wb9DYrjcoKAC>> (Wiley, 2008) (cit. on p. 3).
2. Wu, C. S., Ambler, E., Hayward, R. W., Hoppes, D. D. & Hudson, R. P. Experimental Test of Parity Conservation in Beta Decay. *Phys. Rev.* **105**, 1413–1415 (Feb. 1957) (cit. on p. 3).
3. Christenson, J. H., Cronin, J. W., Fitch, V. L. & Turlay, R. Evidence for the π Decay of the K^0 Meson. *Phys. Rev. Lett.* **13**, 138–140 (July 1964) (cit. on p. 3).
4. Anderson, C. D. The Positive Electron. *Phys. Rev.* **43**, 491–494 (Mar. 1933) (cit. on p. 3).
5. Dirac, P. A. M. The Quantum Theory of the Electron. *Proceedings of the Royal Society of London A: Mathematical, Physical and Engineering Sciences* **117**, 610–624. ISSN: 0950-1207 (1928) (cit. on p. 3).
6. Chamberlain, O., Segrè, E., Wiegand, C. & Ypsilantis, T. Observation of Antiprotons. *Phys. Rev.* **100**, 947–950 (Nov. 1955) (cit. on p. 3).
7. Cork, B., Lambertson, G. R., Piccioni, O. & Wenzel, W. A. Antineutrons Produced from Antiprotons in Charge-Exchange Collisions. *Phys. Rev.* **104**, 1193–1197 (Nov. 1956) (cit. on p. 3).
8. Massam, T., Muller, T., Righini, B., Schneegans, M. & Zichichi, A. Experimental observation of antideuteron production. *Il Nuovo Cimento A* **63**, 10–14. ISSN: 1826-9869 (1965) (cit. on p. 3).
9. Antipov, Y. *et al.* Observation of antihelium-3. *Nuclear Physics B* **31**, 235–252. ISSN: 0550-3213 (1971) (cit. on p. 3).
10. Agakishiev, H. *et al.* Observation of the antimatter helium-4 nucleus. *Nature* **473**, 353–356. ISSN: 0028-0836 (May 2011) (cit. on p. 3).
11. Lombardi, A. M., Pirkl, W. & Bylinsky, Y. *First operating experience with the CERN decelerating RFQ for antiprotons in PACS2001. Proceedings of the 2001 Particle Accelerator Conference (Cat. No.01CH37268)* **1** (2001), 585–587. doi:10.1109/PAC.2001.987575 (cit. on pp. 3, 13).
12. Hori, M. in *CPT and Lorentz Symmetry* 11–14 (World Scientific, Dec. 2010). ISBN: 978-981-4327-67-1. doi:doi : 10.1142/9789814327688_0003. <https://doi.org/10.1142/9789814327688%7B%5C_%7D0003> (cit. on p. 4).

13. Widmann, E. in *CPT and Lorentz Symmetry* 105–108 (World Scientific, Aug. 2016). ISBN: 978-981-314-849-9. doi:doi : 10 . 1142/9789813148505_0027. <https://doi.org/10.1142/9789813148505%7B%5C_%7D0027> (cit. on p. 4).
14. Kellogg, J. M. B., Rabi, I. I. & Zacharias, J. R. The Gyromagnetic Properties of the Hydrogens. *Phys. Rev.* **50**, 472–481 (5 Sept. 1936) (cit. on pp. 4, 12).
15. Colladay, D. & Kostelecký, V. A. Lorentz-violating extension of the standard model. *Phys. Rev. D* **58**, 116002 (Oct. 1998) (cit. on p. 4).
16. Diermaier, M. *et al.* In-beam measurement of the hydrogen hyperfine splitting and prospects for antihydrogen spectroscopy. *Nat. Commun.* **8**, 15749 (June 2017) (cit. on pp. 4, 6).
17. Kolbinger, B. *PhD Thesis (in preparation)* PhD thesis (Universität Wien, 2018) (cit. on pp. 4, 20, 63, 64).
18. Nagata, Y. *et al.* A non-segmented BGO crystal disk with two dimensional readout for an antihydrogen beam detector and data analysis for antihydrogen identification. *in preparation* (2017) (cit. on pp. 4, 20).
19. Hellwig, H. *et al.* Measurement of the Unperturbed Hydrogen Hyperfine Transition Frequency. *IEEE Transactions on Instrumentation and Measurement* **19**, 200–209. ISSN: 0018-9456 (Nov. 1970) (cit. on p. 6).
20. Karshenboim, S. G. Some possibilities for laboratory searches for variations of fundamental constants. *Canadian Journal of Physics* **78**, 639–678 (2000) (cit. on p. 6).
21. Ramsey, N. F. Experiments with separated oscillatory fields and hydrogen masers. *Rev. Mod. Phys.* **62**, 541–552 (3 July 1990) (cit. on p. 6).
22. Lundmark, R. *et al.* Towards a precise measurement of the antihydrogen ground state hyperfine splitting in a beam: the case of in-flight radiative decays. *Journal of Physics B: Atomic, Molecular and Optical Physics* **48**, 184001 (2015) (cit. on p. 8).
23. Kostelecký, V. A. & Vargas, A. J. Lorentz and CPT tests with hydrogen, antihydrogen, and related systems. *Phys. Rev. D* **92**, 056002 (5 Sept. 2015) (cit. on p. 7).
24. Hori, M., Yamashita, K., Hayano, R. & Yamazaki, T. Analog Cherenkov detectors used in laser spectroscopy experiments on antiprotonic helium. *Nuclear Instruments and Methods in Physics Research Section A: Accelerators, Spectrometers, Detectors and Associated Equipment* **496**, 102–122. ISSN: 0168-9002 (2003) (cit. on p. 9).
25. Olive, K. *et al.* Review of Particle Physics. *Chinese Physics C* **38**, 1–1676 (2014) (cit. on p. 10).
26. Moser, S., Harder, W., Hurlbut, C. & Kusner, M. Principles and practice of plastic scintillator design. *Radiation Physics and Chemistry* **41**, 31–36. ISSN: 0969-806X (1993) (cit. on p. 10).
27. Sauerzopf, C. *The ASACUSA antihydrogen detector, development and data analysis* PhD thesis (Technische Universität Wien, 2016). <<http://katalog.ub.tuwien.ac.at/AC13221831>> (cit. on pp. 12, 18, 20, 40, 42–45, 57, 76–78, 80, 81).

28. Capon, A. *Construction of a scintillating hodoscope detector for measurements on the hyperfine structure of antihydrogen* MA thesis (Universität Wien, Wien, 2016). <<http://ubdata.univie.ac.at/AC13295456>> (cit. on pp. 12, 18, 20, 42, 45, 70).
29. Widmann, E. *et al.* Measurement of the hyperfine structure of antihydrogen in a beam. *Hyperfine Interactions* **215**, 1–8. ISSN: 03043843 (2013) (cit. on p. 12).
30. Malbrunot, C. *et al.* Spectroscopy apparatus for the measurement of the hyperfine structure of antihydrogen. *Hyperfine Interactions* **228**, 61–66. ISSN: 03043843 (2014) (cit. on p. 12).
31. W. G. Thomason, J., Garoby, R., Gilardoni, S., J. Jenner, L. & Pasternak, J. Proton driver scenarios at CERN and Rutherford Appleton Laboratory. **16** (May 2013) (cit. on p. 14).
32. Hori, M. & Walz, J. Physics at CERN’s Antiproton Decelerator. *Prog. Part. Nucl. Phys.* **72**, 206–253 (2013) (cit. on pp. 13, 14).
33. Kuroda, N. *Accumulation of a large number of antiprotons and production of an ultra-slow antiproton beam* PhD thesis (University of Tokyo, 2003). <<https://radphys4.c.u-tokyo.ac.jp/theses/PhD/Kuroda-dthes.pdf>> (cit. on p. 13).
34. Nagata, Y. & Yamazaki, Y. A novel property of anti-Helmholz coils for in-coil syntheses of antihydrogen atoms: formation of a focused spin-polarized beam. *New Journal of Physics* **16**, 083026 (2014) (cit. on pp. 13, 16).
35. Kuroda, N. *et al.* A source of antihydrogen for in-flight hyperfine spectroscopy. *Nature communications* **5**. ISSN: 2041-1723. doi:10.1038/ncomms4089 (2014) (cit. on pp. 16, 18).
36. Radics, B. *et al.* The ASACUSA Micromegas Tracker: A cylindrical, bulk Micromegas detector for antimatter research. eng. *The Review of scientific instruments* **86**, 83304. ISSN: 1089-7623 (Electronic) (Aug. 2015) (cit. on p. 16).
37. Nagata, Y. *et al.* *Progress of Antihydrogen Beam Production Using a Double Cusp Trap in Proceedings of the 12th International Conference on Low Energy Antiproton Physics (LEAP2016)* (2017). doi:10.7566/JPSCP.18.011007. <<http://journals.jps.jp/doi/abs/10.7566/JPSCP.18.011007>> (cit. on p. 17).
38. Sauerzopf, C. *et al.* Towards measuring the ground state hyperfine splitting of antihydrogen – a progress report. *Hyperfine Interactions* **237**, 103. ISSN: 1572-9540 (June 2016) (cit. on pp. 18, 19).
39. Federmann, S. *A Spin-Flip Cavity for Microwave Spectroscopy of Antihydrogen* PhD thesis (Universität Wien, 2012). <<http://ubdata.univie.ac.at/AC11008755>> (cit. on p. 18).
40. Nagata, Y. *et al.* Direct detection of antihydrogen atoms using a BGO crystal. *Nuclear Instruments and Methods in Physics Research Section A: Accelerators, Spectrometers, Detectors and Associated Equipment* **840**, 153–159. ISSN: 0168-9002 (2016) (cit. on p. 18).

41. *EJ-200 Plastic Scintillator* 2015. <<http://fcomp.ist.utl.pt/LRC.web/equipamento/EJ200-datasheet.pdf>> (cit. on pp. 18, 20).
42. *Saint Gobain Plastic Scintillating Optical Fibers Brochure* (2017). <https://www.crystals.saint-gobain.com/sites/imdf.crystals.com/files/documents/sgc-scintillation-fiber_0.pdf> (cit. on pp. 26, 71).
43. *KETEK Product Data Sheet SiPM PM3350-EB* (2017). <<https://4b0vz81vun5u2kaw7x3w6pt1-wpengine.netdna-ssl.com/wp-content/uploads/2017/01/KETEK-PM3325-EB-PM3350-EB-Datasheet.pdf>> (cit. on pp. 26, 71).
44. PSI, TRIUMF. *MIDAS wiki* 2017. <https://midas.triumf.ca/MidasWiki/index.php/Main_Page> (cit. on p. 41).
45. Brun, R. & Rademekers, F. ROOT - An Object Oriented Data Analysis Framework. *Nucl. Inst. & Meth. in Phys. Res. A* **389**, 81–86 (1997) (cit. on p. 44).
46. Sauerzopf, C. *waveformlibrary v1.0.0* 2015. doi:10.5281/zenodo.35341. <<https://doi.org/10.5281/zenodo.35341>> (cit. on p. 44).
47. Sauerzopf, C., Gruber, L., Suzuki, K., Zmeskal, J. & Widmann, E. Intelligent Front-end Electronics for Silicon photodetectors (IFES). *Nucl. Instrum. Methods Phys. Res. Sect. A-Accel. Spectrom. Dect. Assoc. Equip.* **819**, 163–166 (cit. on p. 45).
48. CERN/ECP-MIC. *HPTDC Manual* <<https://cds.cern.ch/record/1067476/files/ce-002723234.pdf>> (cit. on p. 46).
49. CAEN. *V1190A/B manual* <<http://www.caen.it/csite/CaenProd.jsp?parent=11%7B%5C%7Ddidmod=785>> (cit. on pp. 49, 52, 55).
50. BeagleBoard.org Foundation. *BeagleBoard website* 2017. <<https://beagleboard.org/>> () (cit. on p. 60).
51. Raspberry PI Foundation. *Raspberry PI website* 2017. <<https://www.raspberrypi.org/>> (cit. on p. 60).

Acknowledgements

Zu Beginn möchte ich Eberhard und dem ganzen SMI von ganzem Herzen danken. Meine Zeit am SMI hat mir viele Chancen gegeben, Neues zu lernen und vielzählige Möglichkeiten eröffnet. Unter den Kollegen will ich speziell auch Bernadette, Clemens, Manfred, Martin und Hannes hervorheben, die mich stets unterstützt und nötigenfalls korrigiert haben. Besonders danken möchte ich auch Hans, ohne den ich gar nicht erst auf das SMI gestossen wäre, und Julia, die stets hilfsbereit war und sich um alle Probleme gekümmert hat. Sehr zu schätzen weiss ich auch die Unterstützung des Werkstatt-Teams während der Konstruktionsphase des Detektors, allen voran Doris, Leo und Mark. An dieser Stelle sollen auch Lukas und Michael erwähnt sein, die Bernadette und mich bei den vorbereitenden Messungen und dem Zusammenbau unterstützt haben.

Weiters möchte ich auch meinen Freunden in Weiz, Wien, und im Ausland danken, die mich stets auch unterstützt haben, und auch trotz meiner langen Abwesenheiten am CERN stets Zeit für mich hatten. Speziell erwähnen will ich an dieser Stelle Martin, Matthias, Wolfgang, Anton, Ulrich, Bernadette, Marlene und Moseph, sowie die Wirt- und Kundschaft vom Cafe Espresso Luis.

Zu guter Letzt will ich meinen Eltern Doris und Ferdinand von ganzen Herzen danken. Ohne eure ständige Unterstützung in emotionaler und materieller Hinsicht wäre all dies niemals möglich gewesen.